

Bonding in the helium dimer in strong magnetic fields: the role of spin and angular momentum

Jon Austad,¹ Alex Borgoo,¹ Erik I. Tellgren,^{1,*} and Trygve Helgaker^{1,†}

¹*Hylleraas Centre for Quantum Molecular Sciences, Department of Chemistry, University of Oslo, P.O. Box 1033 Blindern, N-0315 Oslo, Norway*

We investigate the helium dimer in strong magnetic fields, focusing on the spectrum of low-lying electronic states and their dissociation curves, at the full configuration-interaction level of theory. To address the loss of cylindrical symmetry and angular momentum as a good quantum number for nontrivial angles between the bond axis and magnetic field, we introduce the almost quantized angular momentum (AQAM) and show that it provides useful information about states in arbitrary orientations. In general, strong magnetic fields dramatically rearrange the spectrum, with the orbital Zeeman effect bringing down states of higher angular momentum below the states with pure σ character as the field strength increases. In addition, the spin Zeeman effect pushes triplet states below the lowest singlet; in particular, a field of one atomic unit is strong enough to push a quintet state below the triplets. In general, the angle between the bond axis and the magnetic field also continuously modulates the degree of σ , π , and δ character of bonds and the previously identified perpendicular paramagnetic bonding mechanism is found to be common among excited states. Electronic states with preferred skew field orientations are identified and rationalized in terms of permanent and induced electronic currents.

I. INTRODUCTION

It has long been known that strong magnetic fields dramatically affect the physics and chemistry of molecules [1, 2]. In the atmospheres of neutron stars, intense magnetic fields, orders of magnitudes stronger than one atomic unit $B_0 = 235$ kT, dominate the electrostatic forces, resulting in highly prolate, or even needle-like, charge distributions around atoms. In such ultrastrong magnetic fields, matter is expected to consist of long chains of atoms, oriented parallel to the magnetic field vector. The strong field regime $0.1B_0 < B < B_0$ is interesting as the direct magnetic effects and electrostatic forces in small molecules are on the same order of magnitude, leading to novel and complicated bonding mechanisms. This regime corresponds to the upper range of magnetic field strengths encountered in magnetic white dwarf (MWD) stars.

In the strong and ultrastrong field regimes, atomic spectra and chemical bonding become modified. Calculated helium spectra have assisted the interpretation of observed spectra from the atmosphere of MWDs [3, 4], supplementing the well-established use of hydrogen lines to analyse MWDs. The magnetic field dependence of energy levels in hydrogen [5], hydrogen anions [6], helium [7–9], and other small atoms [10–13] have been subject to several studies. Even one-electron molecular ions exhibit a rich phenomenology to explore [14]. Many otherwise unstable few-electron ions, such as He^- , HeH^+ , and He_2^{2+} , become stabilized in external magnetic fields [15–17]. Several studies have focused on potential-energy surfaces and the modification of bonding in H_2^+ and H_2 subject to strong fields [18–22]. Most

studies have been restricted to the parallel orientation as this is by far the easiest to study. However, a few studies of varying accuracy have found that the H_2 triplet state becomes stabilized in a perpendicular magnetic field [23–27], subsequently explained based on high-quality quantum-chemical calculations as an orientation-dependent stabilization of the antibonding σ -orbital [28]. This effect, termed perpendicular paramagnetic bonding, is also seen in singlet helium clusters and other diatomic molecules [29, 30].

While the highest field strengths available in the laboratory are two to three orders of magnitude below B_0 [31–34], quasiparticles in semiconductors can have effective masses much below that of a bare electron and exhibit analogous effects at lower field strengths. Notably, quasiparticle analogues to perpendicular paramagnetic bonding have already been reported [35, 36]. Rydberg states, which are sensitive to magnetic fields due to their diffuseness and high angular momenta [37, 38], are another promising candidate for analogous effects.

In what follows, we report a computational study of the chemical bonding of the helium dimer. Potential-energy surfaces are mapped for low-lying states of singlet, triplet, and quintet total spin, subject to strong magnetic fields of arbitrary orientation. We use a finite-field approach, where the magnetic-field effects are incorporated directly without perturbative approximations. Although higher-order perturbation theory is sometimes an alternative to probe high-field effects [39–44], a nonperturbative approach is needed to study reliably potential-energy surfaces and level crossings in a strong field. To handle the gauge-origin problem and ensure faster basis-set convergence, we employ London atomic orbitals [45–48]. Without a solution the gauge-origin problem, potential-energy surfaces suffer from a spurious parabolic distance dependence and become qualitatively wrong in a magnetic field. Unlike perturbative approaches, the

* erik.tellgren@kjemi.uio.no

† t.u.helgaker@kjemi.uio.no

present non-perturbative approach necessitates an unconventional integral evaluation scheme, such as the one reported for the LONDON program package [49, 50] or the subsequent approaches in the BAGEL [51], QUEST [52], and CHRONUSQ [53, 54] packages. For the smallest systems, the extremely accurate free-complement method is also an option [55, 56].

The outline of this article is as follows. First, in Sec. II, we specify the electronic Hamiltonian and the quantum-chemical model. We also introduce a new way to classify electronic states and discuss perpendicular paramagnetic bonding involving higher-angular-momentum states. Moreover, we discuss a simple analytical model that gives insight into bonding in strong fields. In Sec. III, we present results for singlet, triplet, and quintet states of the helium dimer in a strong magnetic field. Finally, we summarize the conclusions in Sec. V.

II. THEORY

In the presence of a uniform magnetic field \mathbf{B} , the standard nonrelativistic Hamiltonian for N electrons is in SI-based atomic units given by

$$\hat{H} = \frac{1}{2} \sum_{j=1}^N \hat{\pi}_j^2 + \sum_{j=1}^N \mathbf{B} \cdot \hat{\mathbf{S}}_j + \sum_{j=1}^N v(\mathbf{r}_j) + \sum_{j<l} \frac{1}{r_{jl}}. \quad (1)$$

where $\hat{\mathbf{S}}_j$ is the spin operator for the j th electron, $v(\mathbf{r}_j)$ is the electrostatic potential from the nuclei at the position of the j th electron, $\hat{\pi}_j = -i\nabla_j + \mathbf{A}(\mathbf{r}_j)$ is the mechanical momentum operator, to be distinguished from the canonical momentum operator $\hat{\mathbf{p}}_j = -i\nabla_j$, and $\mathbf{A}(\mathbf{r}_j)$ is the magnetic vector potential at \mathbf{r}_j . Restriction of the vector potential to the linear form $\mathbf{A}(\mathbf{r}) = \frac{1}{2}\mathbf{B} \times (\mathbf{r} - \mathbf{G})$ reduces the gauge freedom to the position of the gauge origin \mathbf{G} .

An efficient way to handle this gauge-origin freedom is to use London atomic orbitals [45–48], leading to gauge-origin invariant results and faster basis-set convergence; see Ref. [57] for a more general perspective. Given a Gaussian-type orbital $\chi(\mathbf{r})$ centred at \mathbf{C} , the corresponding London atomic orbital is $\omega(\mathbf{r}) = e^{-i\mathbf{A}(\mathbf{C}) \cdot \mathbf{r}} \chi(\mathbf{r})$. Hence, ω is product of a Gaussian and a plane wave with wave vector $\mathbf{q} = \mathbf{A}(\mathbf{C})$. The resulting nonstandard integrals, including the two-electron four-centre Coulomb integrals, are evaluated using the LONDON program [49, 50]. This program package also contains a number of electronic structure models [28, 30, 58–60]. We here use the full configuration-interaction (FCI) model [28] to be able to handle exact degeneracies and quasidegeneracies that inevitably arise when parameters such as bond distances and external magnetic fields are varied over large intervals.

A. Classification of states using an approximately quantized angular momentum

In the present section, we shall not be concerned with the spin contribution to angular momentum. For a given state Ψ , the gauge-invariant, physical angular momentum relative to a point \mathbf{D} may then be defined as $\mathbf{J}_{\mathbf{D}} = \langle \Psi | \sum_j (\mathbf{r}_j - \mathbf{D}) \times \hat{\pi}_j | \Psi \rangle$. In fact, since $\langle \Psi | \sum_j \hat{\pi}_j | \Psi \rangle$ vanishes in the complete basis-set limit for any variationally optimized state, the physical angular momentum is independent of the reference point. The gauge-dependent, canonical angular momentum is likewise given by the expectation value $\mathbf{L}_{\mathbf{D}} = \langle \Psi | \sum_j (\mathbf{r}_j - \mathbf{D}) \times \hat{\mathbf{p}} | \Psi \rangle$. Introducing the density and paramagnetic current density,

$$\rho(\mathbf{r}) = \sum_{j=1}^N \langle \Psi | \delta(\mathbf{r} - \mathbf{r}_j) | \Psi \rangle, \quad (2)$$

$$\mathbf{j}_{\mathbf{p}}(\mathbf{r}) = \frac{1}{2} \sum_{j=1}^N \langle \Psi | \delta(\mathbf{r} - \mathbf{r}_j) \hat{\mathbf{p}}_j + \hat{\mathbf{p}}_j \delta(\mathbf{r} - \mathbf{r}_j) | \Psi \rangle, \quad (3)$$

the canonical momentum can also be calculated as $\mathbf{L}_{\mathbf{D}} = \int (\mathbf{r} - \mathbf{D}) \times \mathbf{j}_{\mathbf{p}} d\mathbf{r}$. Under a gauge transformation with gauge function f , we have $\mathbf{A} \mapsto \mathbf{A} + \nabla f$, $\mathbf{j}_{\mathbf{p}} \mapsto \mathbf{j}_{\mathbf{p}} - \rho \nabla f$, and $\mathbf{L}_{\mathbf{D}} \mapsto \mathbf{L}_{\mathbf{D}} - \int (\mathbf{r} - \mathbf{D}) \times \rho \nabla f d\mathbf{r}$. Despite its gauge dependence, the canonical angular momentum is sometimes useful for classifying states.

When both the electrostatic potential and the magnetic vector potential are cylindrically symmetric, the component of $\mathbf{L}_{\mathbf{G}}$ parallel to the symmetry axis is a good quantum number. In general, for a diatomic molecule in a non-parallel magnetic field, canonical momentum ceases to be a good quantum number—also the dissociation limit, since the total system is not cylindrically symmetric even though cylindrical symmetry is restored for the individual subsystems (dissociated atoms). Unlike the physical angular momentum, the canonical momentum depends on a global reference position. To restore quantization in the dissociation limit, the angular momentum of a subsystem instead needs to be evaluated with respect to the symmetry centre of that subsystem, and the wave function must be gauge transformed to correspond to what is obtained in a calculation with gauge origin adapted to the subsystem.

We now consider the idealized case where each isolated subsystem α is cylindrically symmetric about its electronic centre of mass \mathbf{C}_{α} . In a calculation of the isolated system, with the gauge origin placed at \mathbf{C}_{α} , the resulting density ρ_{α} and paramagnetic current density $\mathbf{j}'_{\mathbf{p};\alpha}$ are cylindrically symmetric too. Moreover, the canonical angular momentum relative to \mathbf{C}_{α} is

$$\mathbf{L}'_{\alpha} = \int (\mathbf{r} - \mathbf{C}_{\alpha}) \times \mathbf{j}'_{\mathbf{p};\alpha}(\mathbf{r}) d\mathbf{r}, \quad (4)$$

and the component parallel to \mathbf{B} is quantized. In the limit of a complete basis, the mechanical linear momentum must vanish for any energy eigenstate. Using the

fact that \mathbf{C}_α is the subsystem centre of mass, we see that the paramagnetic and diamagnetic contributions must vanish separately,

$$\begin{aligned}\boldsymbol{\pi}_\alpha &= \int (\mathbf{j}'_{\text{p};\alpha}(\mathbf{r}) + \frac{1}{2}\rho_\alpha(\mathbf{r}) \mathbf{B} \times (\mathbf{r} - \mathbf{C}_\alpha)) d\mathbf{r} \\ &= \int \mathbf{j}'_{\text{p};\alpha}(\mathbf{r}) d\mathbf{r} = \mathbf{0}.\end{aligned}\quad (5)$$

Next, consider the total system. The gauge origin \mathbf{G} cannot coincide with all subsystem centres \mathbf{C}_α . Hence, the subsystem paramagnetic current densities obtained from a calculation on the total systems are gauge transformed according to

$$\mathbf{j}_{\text{p};\alpha}(\mathbf{r}) = \mathbf{j}'_{\text{p};\alpha}(\mathbf{r}) + \frac{1}{2}\rho_\alpha(\mathbf{r}) \mathbf{B} \times (\mathbf{G} - \mathbf{C}_\alpha). \quad (6)$$

The subsystem contribution to the total angular momentum about a global reference point \mathbf{D} thus becomes

$$\mathbf{L}_{\mathbf{D},\alpha} = \int (\mathbf{r} - \mathbf{D}) \times \mathbf{j}_{\text{p};\alpha}(\mathbf{r}) d\mathbf{r}, \quad (7)$$

or, using the relations established above,

$$\begin{aligned}\mathbf{L}_{\mathbf{D},\alpha} &= \int \left((\mathbf{r} - \mathbf{D}) \times \mathbf{j}'_{\text{p};\alpha}(\mathbf{r}) \right. \\ &\quad \left. + \frac{1}{2}\rho_\alpha(\mathbf{r}) (\mathbf{r} - \mathbf{D}) \times (\mathbf{B} \times (\mathbf{G} - \mathbf{C}_\alpha)) \right) d\mathbf{r}.\end{aligned}\quad (8)$$

Writing $N_\alpha = \int \rho_\alpha(\mathbf{r}) d\mathbf{r}$ for the number of electrons in a subsystem and using Eq. (5), we obtain in the basis-set limit

$$\mathbf{L}_{\mathbf{D},\alpha} = \mathbf{L}'_\alpha + \frac{N_\alpha}{2} (\mathbf{C}_\alpha - \mathbf{D}) \times (\mathbf{B} \times (\mathbf{G} - \mathbf{C}_\alpha)). \quad (9)$$

Whereas the total canonical angular momentum

$$\mathbf{L}_{\mathbf{D}} = \sum_\alpha \mathbf{L}_{\mathbf{D},\alpha} \quad (10)$$

exhibits a gauge-dependent quadratic growth with the distances $|\mathbf{C}_\alpha - \mathbf{C}_\beta|^2$ between different subsystems, we can now subtract the quadratic terms to obtain

$$\begin{aligned}\boldsymbol{\Lambda} &= \sum_\alpha \left(\mathbf{L}_{\mathbf{D},\alpha} - \frac{N_\alpha}{2} (\mathbf{C}_\alpha - \mathbf{D}) \times (\mathbf{B} \times (\mathbf{G} - \mathbf{C}_\alpha)) \right) \\ &= \sum_\alpha \mathbf{L}'_\alpha.\end{aligned}\quad (11)$$

We term $\boldsymbol{\Lambda}$ the *approximately quantized angular momentum* (AQAM) since, for a diatomic molecule, its projection $\Lambda_{\mathbf{B}} = \mathbf{e}_{\mathbf{B}} \cdot \boldsymbol{\Lambda}$ onto the field direction $\mathbf{e}_{\mathbf{B}} = \mathbf{B}/|\mathbf{B}|$ exhibits exact quantization for all parallel orientations as well as in the dissociation limit. In other cases, $\Lambda_{\mathbf{B}}$ is often approximately quantized, despite the presence of interactions between subsystems. This quantity therefore provides a useful generalization of the atomic quantum number m_l for classifying the states of a diatomic

TABLE I. Symmetries and bonding properties of molecular orbitals of homonuclear diatomic molecule in a magnetic field. The symbol \angle here indicates an intermediate angle.

$D_{\infty h}$ $B=0$	$C_{\infty h}$ B_{\parallel}	C_{2h} B_{\perp}	C_i B_{\angle}	united-atom limit	preferred orientation	chemical bonding
σ_g^+	σ_g	a_g	a_g	s	\parallel	covalent
σ_u^+	σ_u	b_u	a_u	p ₀	\perp	magnetic
π_u	π_u	$a_u + b_u$	a_u	p $_{\pm 1}$	\parallel	covalent
π_g	π_g	$a_g + b_g$	a_g	d $_{\pm 1}$	\angle	magnetic
δ_g	δ_g	$a_g + b_g$	a_g	d $_{\pm 2}$	\parallel	covalent
δ_u	δ_u	$a_u + b_u$	a_u	f $_{\pm 2}$	\angle	magnetic

molecule. A closely related quantity was considered for a different purpose (and with different notation) in a formal density-functional context in Sec. IV.C of Ref. [61].

Finally, we remark that some care is required when interpreting $\frac{1}{2}\mathbf{B} \cdot \boldsymbol{\Lambda}$ as an energy. The physical angular momentum is a sum of two terms: the canonical angular momentum and the diamagnetic contribution. However, the gauge invariant kinetic energy is a sum of three terms: the canonical kinetic energy, the orbital Zeeman term, and the diamagnetic term. Only one of these terms (and the sum of the other two) can be modified to have a well-defined dissociation limit, not all three simultaneously.

B. Symmetry properties of molecular orbitals

In a magnetic field, the point-group symmetry of He_2 is lower than the symmetry $D_{\infty h}$ of the molecule in the absence of a field. In all field orientations, inversion symmetry exists and the molecule therefore belongs to the C_i point group with the irreps A_g and A_u . In the parallel and perpendicular field orientations additional symmetry operations exist. In the parallel orientation, rotation about the molecular axis give rise to the $C_{\infty h}$ point group with the one-dimensional irreps Σ_g and Σ_u and the two-dimensional irreps Π_g , Π_u , Δ_g , Δ_u, \dots . The $C_{\infty h}$ symmetry group (which does not occur for molecules in the absence of a magnetic field) differs from $D_{\infty h}$ by the absence of vertical mirror planes and two-fold perpendicular axes. Finally, in the perpendicular field orientation, we have in addition to inversion symmetry a two-fold symmetry axis along the field direction, giving rise to the C_{2h} symmetry group with the A_g , A_u , B_g and B_u irreps.

In Table I, we compare the symmetries of the molecular orbitals in the field orientations and also with the atomic orbitals in the united atoms limit.

C. Perpendicular paramagnetic bonding

Strong magnetic fields can lead to new exotic bonding mechanisms. Previous work has established that the normally unbound lowest triplet state of the H_2 becomes

bound in a perpendicular magnetic field of strength on the order of $B \sim B_0$. Also the lowest singlet state of the He_2 molecule becomes substantially stabilized and the equilibrium bond length substantially compressed in a perpendicular field. The underlying bonding mechanism, termed *perpendicular paramagnetic bonding*, is that the antibonding σ_u^* orbital develops an angular momentum, which leads to an energetic stabilization by the orbital Zeeman effect [28]. This is true even in a minimal basis of only s orbitals, provided that they are equipped with London gauge factors. The magnitude of the angular momentum of σ_u^* vanishes in the parallel orientation and the net energetic effect is largest in the perpendicular orientation at intermediate bond lengths. By contrast, the bonding σ_g orbital does not develop an angular momentum and is not stabilized by this mechanism.

The above considerations generalize and apply in a somewhat stronger form to higher angular-momentum states. In the parallel orientation, a linear combination of atomic orbitals with atomic quantum numbers $|m_l| \leq M$ can never lead to an angular momentum exceeding M . By contrast, this becomes possible in nonparallel orientations. For example, the cc-pVDZ basis has two s orbitals and three p orbitals for each helium atom. In a dimer with the helium atoms placed on the x axis at $(\pm 1, 0, 0)$ bohr, one finds by diagonalizing the canonical angular-momentum operator (relative to the mid-bond position) that the largest perpendicular components are $L_{0,z} = \pm 1.83\hbar$. If we omit the 1s orbitals, the 2s orbitals, and both the 1s and 2s orbitals on the two atoms, we obtain $L_{0,z} = \pm 1.35\hbar$, $L_{0,z} = \pm 1.06\hbar$ and $L_{0,z} = \pm 1.03\hbar$, respectively. With London gauge factors and a perpendicular field $\mathbf{B} = 0.5\hbar\mathbf{e}_z$, the most negative eigenvalue becomes $L_{0,z} = -2.08\hbar$. Hence, some combination of s and p orbitals acquires a d-orbital character when the orientation is changed from parallel to perpendicular, leading to a lower orbital Zeeman energy, which competes with the diamagnetic energy.

In light of the visual similarity of antisymmetric combinations of *real-valued* p orbitals to real valued d orbitals, it may be surprising that s functions play such a large role in the above example—for example, an antisymmetric linear combination of two p_y orbitals centred at different points on the x axis resembles a d_{xy} orbital. We remark, however, that the canonical angular momentum vanishes for all real valued orbitals and the s functions are needed to produce complex-valued orbitals of the right form to represent an angular momentum of about $\pm 2\hbar$.

A simple analytical model provides further insight into magnetic-field effects on bonding and antibonding orbitals in homonuclear diatomic molecules. Let $G_{\ell m}(\mathbf{r}, \alpha, \mathbf{K}, \mathbf{B})$ denote a solid-harmonic Gaussian orbital of exponent α centred at \mathbf{K} and equipped with a London phase factor for the magnetic field \mathbf{B} :

$$G_{\ell m}(\mathbf{r}, \alpha, \mathbf{K}, \mathbf{B}) = c_{\ell, m}(\alpha) \exp\left(-i\left(\frac{1}{2}\mathbf{B} \times \mathbf{K}\right) \cdot \mathbf{r}\right) \times S_{\ell m}(\mathbf{r}_K) \exp\left(-\alpha|\mathbf{r}|_K^2\right). \quad (12)$$

Here $c_{\ell, m}(\alpha)$ is a normalization constant and $S_{\ell m}(\mathbf{r}_K)$

with $\mathbf{r}_K = \mathbf{r} - \mathbf{K}$ is a solid-harmonic function centred at \mathbf{K} of angular-momentum quantum numbers ℓ and m about the z axis.

Consider now the normalized bonding and antibonding orbitals along the z axis:

$$g_{\ell m}^{\pm}(\mathbf{r}, \alpha, \delta, \mathbf{B}) = C_{\ell m}(\delta, \alpha) \times (G_{\ell m}(\mathbf{r}, \alpha, (0, 0, +\delta), \mathbf{B}) \pm G_{\ell m}(\mathbf{r}, \alpha, (0, 0, -\delta), \mathbf{B})), \quad (13)$$

where $C_{\ell m}(\delta, \alpha)$ is a normalization constant. We are interested in the united-atom limits of these orbitals,

$$G_{\ell m}^{\pm}(\mathbf{r}, \alpha, \mathbf{B}) = \lim_{\delta \rightarrow 0^+} g_{\ell m}^{\pm}(\mathbf{r}, \alpha, \delta, \mathbf{B}). \quad (14)$$

Clearly, for the bonding orbitals, we have the field-free standard Gaussian orbital positioned at the origin,

$$G_{\ell m}^+(\mathbf{r}, \alpha, \mathbf{B}) = G_{\ell m}(\mathbf{r}, \alpha), \quad (15)$$

in the notation $G_{\ell m}(\mathbf{r}, \alpha) = G_{\ell m}(\mathbf{r}, \alpha, \mathbf{0}, \mathbf{0})$. For the antibonding orbitals, the limit is less trivial. To illustrate, we consider the special case when the magnetic field is oriented perpendicular to the bonding and antibonding orbitals $\mathbf{B}_x = (B, 0, 0)$. We furthermore set the Gaussian exponent equal to the optimal exponent of a free electron in uniform magnetic field, $\alpha_B = B/4$. For $\ell \leq 1$, we then find

$$G_{0,0}^-(\mathbf{r}, \alpha_B, \mathbf{B}_x) = \sqrt{\frac{B}{2}}(y - iz)G_{0,0}(\mathbf{r}, \alpha_B), \quad (16)$$

$$G_{1,\pm 1}^-(\mathbf{r}, \alpha_B, \mathbf{B}_x) = \sqrt{\frac{B}{3}}(y - iz)G_{1,\pm 1}(\mathbf{r}, \alpha_B), \quad (17)$$

$$G_{1,0}^-(\mathbf{r}, \alpha_B, \mathbf{B}_x) = \sqrt{\frac{B}{4}}(y - iz)G_{1,0}(\mathbf{r}, \alpha_B) - G_{0,0}(\mathbf{r}, \alpha_B). \quad (18)$$

Noting that $[L_x, y - iz] = -\hbar(y - iz)$ we conclude that a magnetic field perpendicular to the antibonding orbital induces a component of the angular momentum about the field axis and perpendicular to the angular momentum about the bond axis. To first order, this will reduce the energy of the antibonding orbital in the united-atom limit relative to the dissociation limit. It is a reasonable assumption that this stabilization of antibonding orbitals occurs at all atomic separations but is stronger the closer the two atoms are to each other—that is, to the united-atom limit.

The total kinetic energy and angular momentum of bonding and antibonding atomic orbitals in the united-atom limit with $\alpha = 1$ are given by

$$T_{\ell m}(\mathbf{B}) = \int G_{\ell m}^{\pm}(\mathbf{r}, 1, \mathbf{B})^* \frac{1}{2}\pi_{\mathbf{B}}^2 G_{\ell m}^{\pm}(\mathbf{r}, 1, \mathbf{B}) \, \mathbf{r}, \quad (19)$$

$$\mathbf{L}_{\ell m}(\mathbf{B}) = \int G_{\ell m}^{\pm}(\mathbf{r}, 1, \mathbf{B})^* \mathbf{L} G_{\ell m}^{\pm}(\mathbf{r}, 1, \mathbf{B}) \, \mathbf{r}, \quad (20)$$

where $\frac{1}{2}\pi_{\mathbf{B}}^2$ is the kinetic-energy operator in the magnetic field and \mathbf{L} the canonical angular-momentum operator. For a fixed Gaussian exponent $\alpha = 1$, we have in Table II

TABLE II. Kinetic energy and angular momentum of bonding and antibonding atomic orbitals in the united-atom limit $G_{\ell,m}^{\pm}$ in a zero magnetic field $\mathbf{B} = \mathbf{0}$ and in the minimizing magnetic field $\mathbf{B} = \mathbf{B}_{\ell m}$. Here $\Delta T_{\ell m}(\mathbf{B}_{\ell m}) = T_{\ell m}(\mathbf{B}_{\ell m}) - T_{\ell m}(\mathbf{0})$ and the components of the angular momentum not listed are zero. Units are E_h for energy, \hbar for angular momentum, and B_0 for magnetic field strength.

	$T_{\ell m}(\mathbf{0})$	$L_{\ell m}^z(\mathbf{0})$	$\Delta T_{\ell m}(\mathbf{B}_{\ell m})$	$L_{\ell m}^x(\mathbf{B}_{\ell m})$	$B_{\ell m}$	$\theta_{\ell m}$
$G_{0,0}^+$	3/2	0	0	0	0	✓
$G_{1,\pm 1}^+$	5/2	±1	-1/2	0	2	(90 ± 90)°
$G_{1,0}^+$	5/2	0	0	0	0	✓
$G_{2,\pm 2}^+$	7/2	±2	-4/3	0	8/3	(90 ± 90)°
$G_{2,\pm 1}^+$	7/2	±1	-1/2	0	2	(90 ± 90)°
$G_{2,0}^+$	7/2	0	0	0	0	✓
$G_{0,0}^-$	5/2	0	-0.3	-0.9	2.6	90°
$G_{1,\pm 1}^-$	7/2	±1	-1.2	-1.0	2.9	(90 ± 35)°
$G_{1,0}^-$	7/2	0	-0.2	-0.8	2.7	90°
$G_{2,\pm 2}^-$	9/2	±2	-2.1	-1.1	3.1	(90 ± 48)°
$G_{2,\pm 1}^-$	9/2	±1	-1.2	-1.2	3.4	(90 ± 32)°
$G_{2,0}^-$	9/2	0	-0.7	-1.4	3.2	90°

calculated the kinetic energy and angular momentum of the bonding and antibonding orbitals in the united-atom limit for zero field $\mathbf{B} = \mathbf{0}$ and for the magnetic field $\mathbf{B} = \mathbf{B}_{\min}$ that minimizes the kinetic energy for $\alpha = 1$:

$$\mathbf{B}_{\ell m} = \underset{\mathbf{B}}{\operatorname{argmin}} T_{\ell m}(\mathbf{B}). \quad (21)$$

In the table, we have also listed $B_{\ell m} = |\mathbf{B}_{\ell m}|$ and the angle $\theta_{\ell m}$ of $\mathbf{B}_{\ell m}$ with the z axis (bond axis). We note that, for a free electron in a magnetic field, the optimal Gaussian exponent is $B/4$; for an electron in an atom or molecule up to field strengths of about B_0 , the electronic wave function responds less directly to the magnetic field strength. In Fig. 1, we have plotted the kinetic energy of the bonding and antibonding orbitals in the united-atom limit in the xz plane.

The first two columns in Table II contains information about the energies and angular momentum in the absence of a magnetic field. The kinetic energy is $(\ell + 3/2)E_h$ and $(\ell + 5/2)E_h$ for bonding and antibonding orbitals, respectively, the higher energy of the antibonding arising from the presence of an additional nodal plane in the orbital.

Turning our attention to the orbitals in the minimizing magnetic field $\mathbf{B}_{\ell m}$, we note that

$$\Delta T_{\ell m}(\mathbf{B}_{\ell m}) = T_{\ell m}(\mathbf{B}_{\ell m}) - T_{\ell m}(\mathbf{0}) \quad (22)$$

is zero or negative. Furthermore, the only orbitals whose global energy minimum occurs at zero field are the bonding orbitals with $m = 0$. For bonding orbitals with $m < 0$, the energy is lowered by applying a field parallel with the quantization axis (bond axis); if $m > 0$, the same minimum energy is obtained by applying a magnetic field of the same magnitude but in the opposite

direction. As expected, the energy minimum becomes deeper and the minimizing field stronger with increasing value of $|m|$. We note that the energy minimization of the bonding orbitals is the same in the united-atom and dissociation limits, being associated with the permanent angular momentum in the system. We also note that, in a sufficiently strong field, the energy of the orbitals will increase diamagnetically, for all field orientations

For antibonding orbitals in the united-atom limit, the energy is in all cases reduced by the magnetic field and in all cases significantly more than for the corresponding bonding orbitals. At the same time, an angular momentum is induced in the direction of the magnetic field, as predicted from Eqs. (16)–(18). The resulting total angular momentum is then no longer parallel to the bond axis and the minimizing magnetic field is no longer parallel or antiparallel to the z axis. Indeed, for orbitals with $m = 0$, the preferred field orientation is perpendicular to the bond axis, while for orbitals with $m \neq 0$, the preferred field orientation is skewed relative to the bond axis. We note that the energy lowering arising from the induced angular momentum vanishes in the dissociation limit, unlike the energy lowering arising from the permanent angular momentum.

III. RESULTS

The spectrum of He_2 depends on the bond length R , the strength of the magnetic field B , and the angle θ between the field and the bond axis. We have employed the LONDON program [49, 50] to map out the spectrum as a function of these parameters. Basis sets are denoted by standard notation amended by prefixes ‘L’ and ‘u’ to indicate London gauge factors and uncontracted functions, respectively. The calculations have been carried out at the FCI/Lu-aug-cc-pVTZ level unless otherwise indicated. All bond distances are reported in units of $a_0 = 1$ bohr.

A. Dissociation limit: helium atom

In the limit of an infinite bond distance, the helium dimer becomes two isolated helium atoms. The atomic spectrum, calculated at the FCI/Lu-aug-cc-pVQZ level, is shown in Fig. 2, with singlet- and triplet-state energies plotted along the negative and positive axes, respectively.

While the diamagnetic $^1\Sigma_g(1s^2)$ singlet state is the lowest singlet in the plotted field interval (and also the ground state up to about $0.8B_0$), the remaining singlets in the plot undergo several level crossings. In particular, due to the orbital Zeeman interaction, the $^1\Pi_u(1s2p_{-1})$ state crosses the $^1\Sigma_g(1s2s)$ state to become the first excited singlet state at about $0.1B_0$. At a magnetic field strength of about $1B_0$, the paramagnetic $^1\Delta_g(1s3d_{-2})$ state has been sufficiently stabilized to become the second excited singlet state, having crossed in turn the four dia-

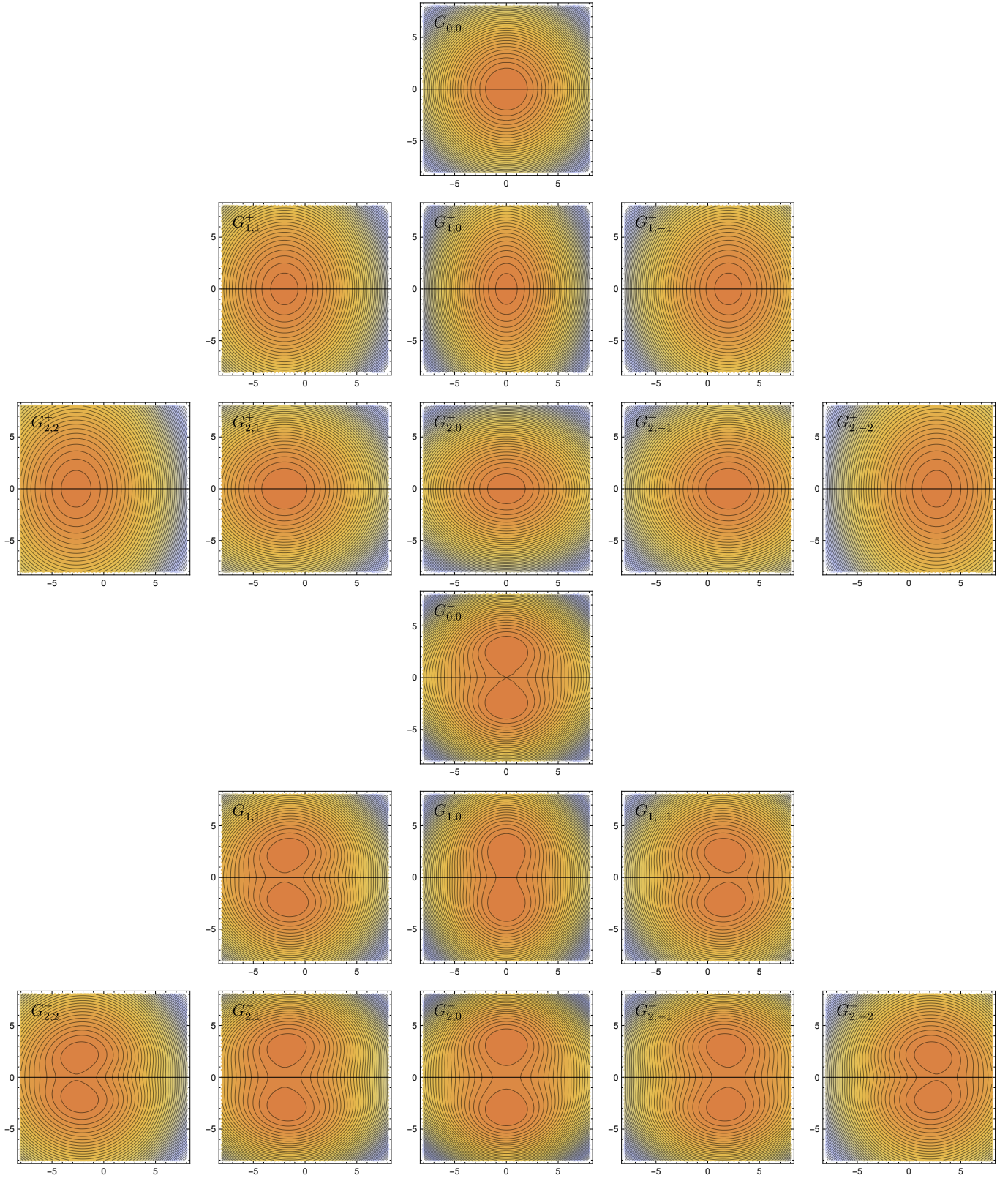


FIG. 1. Contour plots of the kinetic energy of bonding and antibonding orbitals in the united-atom limit as a function of magnetic field strength \mathbf{B} in the zx plane; with the z axis marked by a horizontal line. For bonding orbitals, the minimum is located on the z axis; for the antibonding orbitals, the minima are located away from the z axis, symmetrically on each side.

magnetic states $^1\Sigma_g(1s3s)$, $^1\Pi_u(1s2p_{+1})$, $^1\Sigma_g(1s2s)$, and $^1\Sigma_u(1s2p_0)$ with increasing field strength.

Most singlet states have analogues in the triplet spectrum. However, because of the the spin Zeeman interaction, the triplet states are split, the $m_s = -1$ components (with two spin-down electrons) being stabilized more than the corresponding singlet states. Additional stabilization may be provided by the orbital Zeeman interaction. Thus, while the lowest triplet state is $^3\Sigma_g(1s2s)$ in weak magnetic fields, the $^3\Pi_u(1s2p_{-1})$ state becomes the lowest triplet at $0.2B_0$ and the ground state at about $0.8B_0$. In even stronger fields, the ground state becomes $^3\Delta_g(1s3d_{-2})$, and so on.

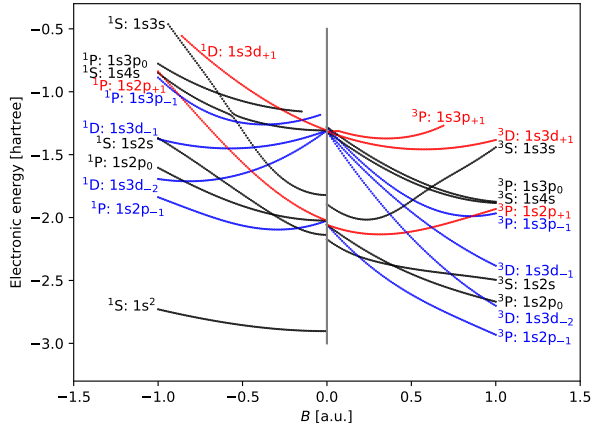


FIG. 2. Spectrum of the helium atom as a function of magnetic field strength. Singlet states are shown along the negative horizontal axis and triplet states along the positive axis.

B. United-atom limit: beryllium atom

It is also instructive to consider the united-atom limit, in which the helium dimer becomes the beryllium atom. The corresponding spectrum, obtained at the FCI/Lucc-pVDZ level of theory, is shown in Fig. 3. Again, the Zeeman interactions result in a reordering of the spectrum. As the zero-field singlet ground state $^1\Sigma_g(1s^22s^2)$ is increasingly destabilized by the magnetic field, the $^1\Delta_g(1s^22p_{-1}^2)$ state becomes the lowest singlet in the strongest fields plotted.

However, because of the spin Zeeman interaction, the $m_s = -1$ triplet components are stabilized even faster. Indeed, already at about $0.05B_0$, the ground state is $^3\Pi_u(1s^22s2p_{-1})$. For the strongest field strengths shown, the first excited state is $^3\Phi_u(1s^22p_{-1}3d_{-2})$, which appears to become the ground state at a field strength slightly stronger than one atomic unit.

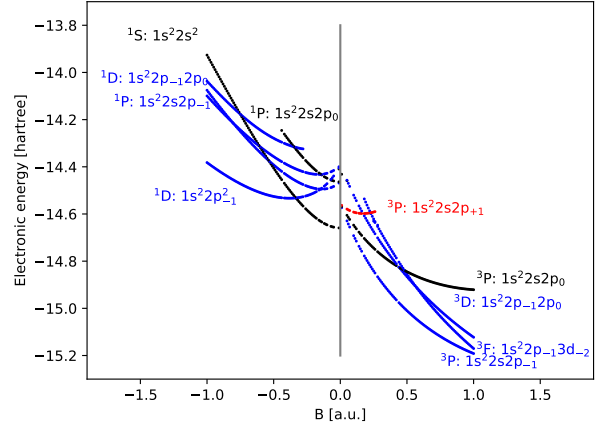


FIG. 3. Spectrum of the beryllium atom as a function of magnetic field strength. Singlet and triplet states are shown along the negative and positive horizontal axes, respectively.

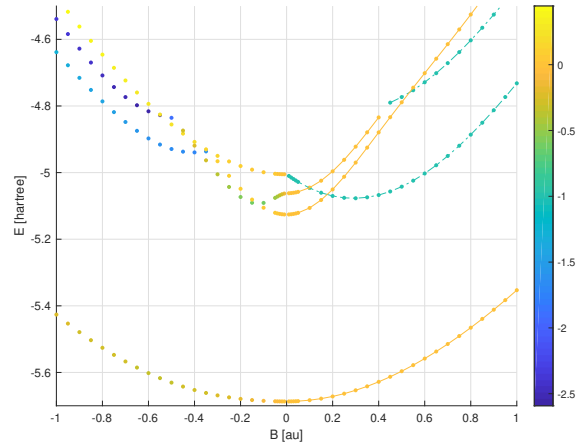


FIG. 4. Singlet spectrum as a function of magnetic field for the He_2 molecule, with fixed bond distance $R = 2a_0$. Perpendicular (parallel) magnetic fields have been mapped to the negative (positive) half of the horizontal axis.

C. States of He_2 at a fixed bond distance $R = 2a_0$

As several interesting minima in the dissociation curves appear at a He–He bond distance of about $R = 2a_0$ (see below), it is instructive to consider the field dependence of the electronic spectrum at this fixed bond length. In the following, we consider the singlet and triplet spectra of He_2 separately. The energies of singlet and triplet states are plotted in Fig. 4 and Fig. 5, respectively, with the energies in the parallel and perpendicular field orientations plotted along the positive and negative axes, respectively.

1. Singlet states of He₂ at $R = 2a_0$

In a parallel field, the four lowest singlet states at $R = 2a_0$ are $^1\Sigma_g(\sigma_{1s}^2\sigma_{1s}^{*2})$, $^1\Sigma_u(\sigma_{1s}^2\sigma_{1s}^*\sigma_{2s})$, and $^1\Sigma_g(\sigma_{1s}^2\sigma_{1s}^*\sigma_{2s}^*)$ with $\Lambda_B = 0$ and $^1\Pi_g(\sigma_{1s}^2\sigma_{1s}^*\pi_{-1})$ with $\Lambda_B = -1$, whose energies are plotted against the field strength along the positive axis in Fig. 4. While the three sigma states are destabilized diamagnetically in the field, the pi state is stabilized and becomes the second singlet state at $B = 0.18B_0$. In fields stronger than about $0.6B_0$, the third singlet is $^1\Pi_u(\sigma_{1s}^2\sigma_{1s}^*\pi_{-1}^*)$, having crossed the two highest sigma states. At this field strength, however, the ground state is no longer a singlet but a triplet, as discussed below.

In the perpendicular field orientation, where the molecular point group is C_{2h} rather than $C_{\infty h}$, the loss of cylindrical spatial symmetry manifests itself in more avoided crossings as seen in Fig. 4, where the energies of the lowest electronic states are plotted against the field strength along the negative axis.

In a weak perpendicular magnetic field, the ground state is $^1A_g(1a_g^21b_u^2)$, while the lowest excited states are $^1B_u(1a_g^21b_u2a_g)$, $^1A_g(1a_g^21b_u2b_u)$, and $^1B_g(1a_g^21b_u1a_u)$. These states originate from the same field-free states as do the lowest states in parallel field orientation except that the third excited state correlates with $^1\Pi_g(\sigma_{1s}^2\sigma_{1s}^*\pi_{||})$, which contains a singly occupied $\pi_{||} = (\pi_+ + \pi_-)/\sqrt{2}$ orbital of a_u symmetry rather than a singly occupied π_{-1} orbital of $a_u + b_u$ symmetry in the C_{2h} point group. Hence, $^1B_g(1a_g^21b_u1a_u)$ is diamagnetic rather than paramagnetic.

Here and in the following, $\pi_{||}$ denotes the π component of symmetry a_u parallel to the magnetic field, whereas π_{\perp} denotes the π component of symmetry b_u perpendicular to the field and bond axes. We likewise use the notation $\pi_{||}^*$ for the π component of symmetry b_g parallel to the magnetic field, whereas π_{\perp}^* denotes the component of symmetry a_g perpendicular to the field and bond axes.

In a perpendicular magnetic field of about $B = 0.15B_0$, $^1A_g(1a_g^21b_u2b_u)$ crosses $^1B_u(1a_g^21b_u2a_g)$ to become the lowest excited state, stabilized by the antibonding 2s orbital in the magnetic field by the paramagnetic bonding mechanism. At a field strength of about $B = 0.35B_0$, the state $^1B_u(1a_g^21b_u3a_g)$, which originates from the high-lying zero-field state $^1\Pi(\sigma_{1s}^2\sigma_{1s}^*\pi_{\perp}^*)$ with a singly occupied π_{\perp}^* orbital of a_g symmetry, goes through a narrowly avoided crossing with the second lowest excited state $^1B_u(1a_g^21b_u2a_g)$. Around this avoided crossing, the $2a_g$ orbital changes character from σ_{2s} to π_{\perp}^* , pushing the second excited state $^1B_u(1a_g^21b_u2a_g)$ further down to recross $^1A_g(1a_g^21b_u2b_u)$, becoming again the first excited state, but with a HOMO of π_{\perp}^* rather than σ_{2s} character.

To summarize, the HOMO of the first excited state in the perpendicular field orientation is σ_{2s} from zero field to $0.15B_0$, then becomes σ_{2s}^* followed by π_{\perp}^* at $0.35B_0$. This progression may be understood in terms of paramagnetic stabilization of the orbitals, noting that the three orbitals have zero, one, and two nodal planes, respectively, par-

allel to the magnetic field vector; see Table II.

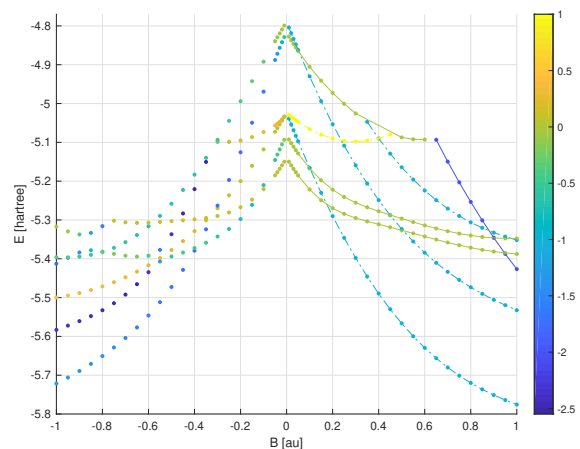


FIG. 5. Triplet spectrum as a function of magnetic field for the He₂ molecule, with fixed bond distance $R = 2a_0$. Perpendicular (parallel) magnetic fields have been mapped to the negative (positive) half of the horizontal axis.

2. Triplet states of He₂ at $R = 2a_0$

The behaviour of the triplet states in parallel and perpendicular fields are plotted along the positive and negative axes of Figure 5, respectively. The triplet states behave in a similar way to the corresponding open-shell singlets except that the spin Zeeman interaction splits the triplet states into three m_s components, the $m_s = -1$ and $m_s = +1$ components tilted downwards and upwards, respectively. We here consider the lowest-energy $m_s = -1$ components only.

Because of the spin Zeeman interaction, the ground state is the singlet $^1\Sigma_g(\sigma_{1s}^2\sigma_{1s}^{*2})$ only up to a field strength of about $0.55B_0$ in the parallel field orientation and about $0.65B_0$ in the perpendicular orientation, where the triplet states $^3\Pi_g(\sigma_{1s}^2\sigma_{1s}^*\pi_{-1})$ and $^3A_u(1a_g^21b_u1b_g)$, respectively, become the ground states, the latter originating from $^3\Pi_u(\sigma_{1s}^2\sigma_{1s}^*\pi_{\perp}^*)$.

In a weak parallel field, with $B \lesssim 0.1B_0$, the two lowest triplet states are $^3\Sigma_u(\sigma_{1s}^2\sigma_{1s}^*\sigma_{2s})$ and $^3\Sigma_g(\sigma_{1s}^2\sigma_{1s}^*\sigma_{2s}^*)$, with $\Lambda_B = 0$. The next two states are $^3\Pi_g(\sigma_{1s}^2\sigma_{1s}^*\pi_{-1})$ and $^3\Pi_g(\sigma_{1s}^2\sigma_{1s}^*\pi_{+1})$, which diverge with increasing field strength due to the orbital Zeeman interaction with opposite signs of $\Lambda_B = \pm 1$. In fields stronger than about $0.5B_0$, the lowest states are completely reordered by the spin and orbital Zeeman interactions. The lowest triplet is now $^3\Pi_g(\sigma_{1s}^2\sigma_{1s}^*\pi_{-1})$, which is also the electronic ground state of the system, while the first excited state is $^3\Pi_u(\sigma_{1s}^2\sigma_{1s}^*\pi_{-1}^*, \sigma_{1s}^{*2}\sigma_{1s}\pi_{-1})$. At one-atomic unit field strength B_0 , the second excited state is $^3\Delta_u(\sigma_{1s}^2\sigma_{1s}^*\delta_{-2})$.

In a weak perpendicular field, the three lowest electronic triplet states are predominantly $^3B_u(1a_g^21b_u2a_g)$,

TABLE III. The lowest minima on dissociation curves for He₂ in a magnetic field $B = 0.2B_0$. The quantity R_{grid} is the bond distance for which the electron configuration, while other quantities are interpolated between grid points on the dissociation curve. All quantities are in atomic units.

spin	θ	n	E_{min}	R_{eq}	$\Lambda_{\mathbf{B}}$	E_{∞}	E_{dis}	state	R_{grid}
singlet	0°	0	-5.786650	5.733	0.00	-5.786619	0.000031	$^1\Sigma_{\text{g}}(0.98\sigma_{1\text{s}}^2\sigma_{1\text{s}}^{*2})$	5.800
		1	-5.070304	1.972	-1.00	-4.934970	0.135334	$^1\Pi_{\text{g}}(0.95\sigma_{1\text{s}}^2\sigma_{1\text{s}}^*\pi_{-1})$	2.000
		2	-5.051661	1.917	0.00	-4.960160	0.091501	$^1\Sigma_{\text{u}}(0.92\sigma_{1\text{s}}^2\sigma_{1\text{s}}^*\sigma_{2\text{s}})$	1.900
	90°	3	-4.996800	2.079	0.00	-4.960157	0.036643	$^1\Sigma_{\text{g}}(0.93\sigma_{1\text{s}}^2\sigma_{1\text{s}}^*\sigma_{2\text{s}}^*)$	2.100
		0	-5.786667	5.271	-0.00	-5.786618	0.000049	$^1\text{A}_{\text{g}}(0.981\text{a}_{\text{g}}^21\text{b}_{\text{u}}^2)$	5.200
		1	-5.073291	2.021	-0.57	-4.959465	0.113826	$^1\text{A}_{\text{g}}(0.881\text{a}_{\text{g}}^21\text{b}_{\text{u}}2\text{b}_{\text{u}})$	2.000
triplet	0°	2	-5.050287	1.896	0.07	-4.959458	0.090829	$^1\text{B}_{\text{u}}(0.921\text{a}_{\text{g}}^21\text{b}_{\text{u}}2\text{a}_{\text{g}})$	1.900
		3	-4.980790	1.946	0.07	unknown	unknown	$^1\text{B}_{\text{g}}(0.951\text{a}_{\text{g}}^21\text{b}_{\text{u}}1\text{a}_{\text{u}})$	1.900
		0	-5.290267	1.966	-1.00	-5.182528	0.107739	$^3\Pi_{\text{g}}(0.95\sigma_{1\text{s}}^2\sigma_{1\text{s}}^*\pi_{-1})$	2.000
	90°	1	-5.270141	1.937	0.00	-5.206973	0.063168	$^3\Sigma_{\text{u}}(0.89\sigma_{1\text{s}}^2\sigma_{1\text{s}}^*\sigma_{2\text{s}})$	1.900
		2	-5.222877	2.103	0.00	-5.206972	0.015905	$^3\Sigma_{\text{g}}(0.88\sigma_{1\text{s}}^2\sigma_{1\text{s}}^*\sigma_{2\text{s}}^*)$	2.100
		0	-5.297553	2.006	-0.68	-5.206769	0.090784	$^3\text{A}_{\text{g}}(0.841\text{a}_{\text{g}}^21\text{b}_{\text{u}}2\text{b}_{\text{u}})$	2.000
90°	1	-5.268197	1.918	0.07	-5.206769	0.061428	$^3\text{B}_{\text{u}}(0.891\text{a}_{\text{g}}^21\text{b}_{\text{u}}2\text{a}_{\text{g}})$	1.900	
	2	-5.200512	1.941	0.07	-5.094688	0.105824	$^3\text{B}_{\text{g}}(0.951\text{a}_{\text{g}}^21\text{b}_{\text{u}}1\text{a}_{\text{u}})$	1.900	
	quintet	0°	0	-4.652235	4.141	-1.00	-4.604572	0.047663	$^5\Pi_{\text{g}}(0.68\sigma_{1\text{s}}\sigma_{1\text{s}}^*\sigma_{2\text{s}}\pi_{-1})$
1			-4.627960	6.052	0.00	-4.626512	0.001448	$^5\Sigma_{\text{g}}(0.73\sigma_{1\text{s}}\sigma_{1\text{s}}^*\sigma_{2\text{s}}\sigma_{2\text{s}}^*)$	6.200
90°		0	-4.686660	4.560	-0.67	-4.627365	0.059295	$^5\text{A}_{\text{g}}(0.441\text{a}_{\text{g}}1\text{b}_{\text{u}}2\text{b}_{\text{u}}3\text{a}_{\text{g}}, 0.321\text{a}_{\text{g}}1\text{b}_{\text{u}}2\text{b}_{\text{u}}2\text{a}_{\text{g}})$	4.600
		1	-4.632662	5.074	-0.59	-4.603487	0.029175	$^5\text{B}_{\text{u}}(0.821\text{a}_{\text{g}}1\text{b}_{\text{u}}2\text{a}_{\text{g}}3\text{a}_{\text{g}})$	5.000
		2	-4.609599	5.648	-0.90	-4.602014	0.007585	$^5\text{A}_{\text{g}}(0.431\text{a}_{\text{g}}1\text{b}_{\text{u}}2\text{b}_{\text{u}}3\text{a}_{\text{g}}, 0.261\text{a}_{\text{g}}1\text{b}_{\text{u}}2\text{b}_{\text{u}}2\text{a}_{\text{g}})$	5.800

$^3\text{A}_{\text{g}}(1\text{a}_{\text{g}}^21\text{b}_{\text{u}}2\text{b}_{\text{u}})$, and $^3\text{B}_{\text{g}}(1\text{a}_{\text{g}}^21\text{b}_{\text{u}}1\text{a}_{\text{u}})$, originating from the field-free states $^3\Sigma_{\text{u}}^+(\sigma_{1\text{s}}^2\sigma_{1\text{s}}^*\sigma_{2\text{s}})$, $^3\Sigma_{\text{g}}^+(\sigma_{1\text{s}}^2\sigma_{1\text{s}}^*\sigma_{2\text{s}}^*)$, and $^3\Pi_{\text{g}}(\sigma_{1\text{s}}^2\sigma_{1\text{s}}^*\pi_{\perp})$. At $0.2B_0$, the lowest two triplet states have crossed and the lowest state is now $^3\text{A}_{\text{g}}(1\text{a}_{\text{g}}^21\text{b}_{\text{u}}2\text{b}_{\text{u}})$; see Table III. In the strongest field plotted in Fig. 5, the ground state is $^3\text{B}_{\text{u}}(1\text{a}_{\text{g}}^21\text{b}_{\text{u}}1\text{a}_{\text{g}})$, originating from the field-free state $^3\Pi_{\text{u}}(\sigma_{1\text{s}}^2\sigma_{1\text{s}}^*\pi_{\perp}^*)$. As the field increases from zero, this highly-excited state drops below all other triplet states, including the $^3\text{B}_{\text{g}}$ state that originates from $^3\Pi_{\text{g}}(\sigma_{1\text{s}}^2\sigma_{1\text{s}}^*\pi_{\text{u}})$. In the process, the $^3\text{B}_{\text{u}}$ state acquires a substantial negative AQAM value from the occupied antibonding $\sigma_{1\text{s}}^*$ and π_{\perp}^* orbitals. Decreasing from 0.50 at field strength $0.01B_0$ to -1.42 at $0.05B_0$, it reaches a minimum value of $\Lambda_{\mathbf{B}} = -1.75$ at $0.25B_0$, after which it increases again to -1.24 at field strength B_0 . We note that the evolution of the lowest triplet state in the perpendicular orientation parallels that of the lowest singlet state, the HOMO changing character first from $\sigma_{2\text{s}}$ to $\sigma_{2\text{s}}^*$ and then from $\sigma_{2\text{s}}^*$ and to π_{\perp}^* .

D. Potential-energy curves of He₂

Next, we explore how the energy spectrum varies with the bond distance R and the field orientation θ . For visualization purposes, energy curves for perpendicular (parallel) orientations will in all cases be plotted with a negative (positive) bond distance. The lowest minima on these dissociation curves are summarized in Table III and IV, for $B = 0.2B_0$ and $B = B_0$, respectively.

At small bond distances, the dissociation curves are dominated by the nuclear electrostatic repulsion energy,

obscuring the united-atom limit. We therefore select a cut-off distance R_{c} , marked with vertical grey dash-dot lines in each figure. In the region $R < R_{\text{c}}$, we replace the actual energy $E(R)$ by a shifted energy

$$E'(R) = E(R) + \frac{Z^2}{R_{\text{c}}} - \frac{Z^2}{R} - a(R - R_{\text{c}})^3 - b(R - R_{\text{c}})^2 - c(R - R_{\text{c}}), \quad (23)$$

more suited to the united-atom limit. The second and third terms remove the singular nuclear repulsion energy, while the polynomial in $R - R_{\text{c}}$ aligns the energy scale. The shift is state independent; it vanishes but introduces nondifferentiable kinks and cusps at the cut-off distance $R = R_{\text{c}}$.

In the united-atom limit, as $R \rightarrow 0$, the molecular orbital basis set becomes linearly dependent, spanning only an orbital space of half the dimension. To avoid spurious results from near linear dependence in this region, we therefore avoid very short bond distances in the dissociation curves.

Finally, we remark that the common notions of bonding and antibonding orbitals, associated with symmetry and antisymmetry with respect to mirror reflection σ_{midbond} in the midbond plane, become more complicated and not well defined in the presence of a magnetic field. While this symmetry remains exact in a parallel field, a nonparallel magnetic fields breaks it. As a result, orbitals become superpositions $\phi = a\phi_{+} + b\phi_{-}$ with $|a|^2 + |b|^2 = 1$ of symmetric and antisymmetric components. The expectation value of the mirror reflection op-

TABLE IV. The lowest minima on dissociation curves for He₂ in a magnetic field $B = B_0$. The quantity R_{grid} is the bond distance for which the electron configuration, while other quantities are interpolated between grid points on the dissociation curve. All quantities are in atomic units.

spin	θ	n	E_{min}	R_{eq}	$\Lambda_{\mathbf{B}}$	E_{∞}	E_{dis}	state	R_{grid}	
singlet	0°	0	-5.454327	4.747	0.00	-5.453984	0.000343	$^1\Sigma_g(0.99\sigma_{1s}^2\sigma_{1s}^{*2})$	4.700	
		1	-4.739260	1.800	-1.00	-4.555238	0.184022	$^1\Pi_g(0.96\sigma_{1s}^2\sigma_{1s}^*\pi_{-1})$	1.800	
		2	-4.554578	4.420	-1.00	-4.554309	0.000269	$^1\Pi_u(0.64\sigma_{1s}^2\sigma_{1s}^*\pi_{-1})$	4.600	
	90°	3	-4.423187	1.893	-2.00	unknown	unknown	$^1\Delta_g(0.96\sigma_{1s}^2\sigma_{1s}^*\delta_{-2})$	1.900	
		0	-5.455252	3.012	-0.00	-5.453983	0.001269	$^1A_g(0.991a_g^21b_u^2)$	3.000	
		1	-4.638450	2.009	-1.27	-4.555000	0.083450	$^1B_u(0.951a_g^21b_u2a_g)$	2.000	
		2	-4.570580	3.136	-1.07	-4.554542	0.016038	$^1A_g(0.761b_u^21a_g2a_g)$	3.200	
		3	-4.503213	1.617	0.24	unknown	unknown	$^1B_g(0.951a_g^21a_u1b_u)$	1.600	
		triplet	0°	0	-5.782268	1.805	-1.00	-5.644685	0.137583	$^3\Pi_g(0.95\sigma_{1s}^2\sigma_{1s}^*\pi_{-1})$
2	-5.428475	1.889	-2.00	unknown	unknown	$^3\Delta_g(0.96\sigma_{1s}^2\sigma_{1s}^*\delta_{-2})$	1.900			
2	-5.404984	2.613	-1.00	-5.256417	0.148567	$^3\Pi_u(0.61\sigma_{1s}^2\sigma_{1s}^*\pi_{-1}, 0.34\sigma_{1s}^2\sigma_{1s}^*\pi_{-1})$	2.600			
2	-5.406632	5.518	0.00	-5.393051	0.013581	$^3\Sigma_u(0.75\sigma_{1s}^2\sigma_{1s}^*\sigma_{2s})$	5.400			
90°	0	-5.721430	1.991	-1.25	-5.644682	0.076748	$^3B_u(0.941a_g^21b_u2a_g)$	2.000		
1	-5.658760	3.245	-1.10	-5.644682	0.014078	$^3A_g(0.701b_u^21a_g2a_g, 0.251a_g^21b_u2b_u)$	3.200			
2	-5.530958	1.611	0.22	-5.393015	0.137943	$^3B_g(0.951a_g^21b_u1a_u)$	1.600			
2	-5.460260	2.416	-1.77	-5.256414	0.203846	$^3A_g(0.581a_g^21b_u2b_u, 0.351b_u^21a_g2a_g)$	2.400			
quintet	0°	0	-5.835333	∞	-2.00	-5.835333	0	$^5\Delta_g(0.92\sigma_{1s}\sigma_{1s}^*\pi_{-1}\pi_{-1}^*)$	10.000	
		1	-5.645344	2.396	-3.00	-5.448259	0.197085	$^5\Phi_u(0.93\sigma_{1s}\sigma_{1s}^*\pi_{-1}\delta_{-2})$	2.400	
		1	-5.650264	4.085	-1.00	-5.583994	0.066270	$^5\Pi_g(0.86\sigma_{1s}\sigma_{1s}^*\pi_{-1}\sigma_{2s})$	4.200	
	90°	0	-5.855142	3.620	-2.21	-5.835368	0.019774	$^5A_g(0.911a_g1b_u2a_g2b_u)$	3.800	
		1	-5.677227	2.660	-0.44	-5.583805	0.093422	$^5B_g(0.891a_g1b_u2a_g1a_u)$	2.600	
		2	-5.618470	3.092	-0.82	-5.583719	0.034751	$^5A_u(0.831a_g1b_u2a_g1b_g)$	3.000	
		3	-5.577629	3.523	-2.83	-5.447773	0.129856	$^5B_u(0.871a_g1b_u2a_g3a_g)$	3.400	

TABLE V. Orbital expectation values s of reflection in the mid-bond plane Eq. (24) for the lowest eight RHF orbitals in He₂ in a perpendicular field of strength B_{\perp} . A value of $s = +1$ implies perfect symmetry and is associated with bonding properties, while a value of $s = -1$ implies perfect antisymmetry and is associated with a nodal plane and antibonding properties. Due to field-induced symmetry breaking, intermediate values are typical, indicating mixing of bonding and antibonding properties. The last row contains the mean absolute s value of the eight listed RHF orbitals for a given bond distance and field strength.

$B_{\perp} = 0.2B_0$				$B_{\perp} = 1.0B_0$							
$R = 2.0a_0$	$R = 3.8a_0$	$R = 5.0a_0$	$R = 5.8a_0$	$R = 1.8a_0$	$R = 2.0a_0$	$R = 2.5a_0$	$R = 3.0a_0$	$R = 3.2a_0$	$R = 3.8a_0$		
1a _g 1.00	1a _g 0.98	1a _g 0.96	1a _g 0.94	1a _g 0.96	1a _g 0.93	1a _g 0.86	1a _g 0.77	1a _g 0.73	1a _g 0.62		
1b _u -0.97	1b _u -0.97	1b _u -0.95	1b _u -0.94	1b _u -0.70	1b _u -0.71	1b _u -0.71	1b _u -0.67	1b _u -0.65	1b _u -0.59		
2b _u 0.12	2b _u 0.17	2b _u 0.23	2b _u 0.26	2a _g 0.08	2a _g 0.12	2a _g 0.25	2a _g 0.37	2a _g 0.40	2a _g 0.42		
2a _g 0.99	2a _g 0.89	2a _g 0.73	2a _g 0.61	2b _u 0.00	2b _u 0.00	2b _u 0.01	2b _u 0.03	2b _u 0.03	2b _u 0.04		
1a _u 0.99	3a _g 0.14	3a _g 0.28	3a _g 0.30	1a _u 0.90	1a _u 0.85	1a _u 0.70	1a _u 0.54	1a _u 0.47	1a _u 0.31		
3a _g -0.11	1a _u 0.95	1a _u 0.88	3b _u 0.06	1b _g 0.14	1b _g 0.13	1b _g 0.12	1b _g 0.12	1b _g 0.12	1b _g 0.10		
3b _u 0.78	3b _u 0.62	3b _u 0.30	1a _u 0.82	3a _g 0.83	3b _u 0.26	3b _u 0.32	3a _g 0.12	3a _g 0.11	3a _g 0.18		
4b _u -0.61	1b _g -0.84	1b _g -0.81	1b _g -0.78	3b _u 0.23	3a _g 0.78	3a _g 0.46	3b _u 0.34	3b _u 0.33	3b _u 0.25		
0.70	0.70	0.64	0.59	0.48	0.47	0.43	0.37	0.36	0.31		

erator,

$$s = \langle \phi | \sigma_{\text{midbond}} | \phi \rangle = |a|^2 - |b|^2, \quad (24)$$

provides a measure of this mixing. In general, a fraction $|a|^2 = \frac{1}{2}(1 + s)$ of ϕ is symmetric and bonding, whereas a fraction $|b|^2 = \frac{1}{2}(1 - s)$ is antisymmetric and antibonding. In Table V, this expectation value is given for several bond distances R and perpendicular field strengths B_{\perp} for the reference restricted Hartree–Fock (RHF) orbitals employed in the FCI calculations. Note that the triplet and quintet states were also calculated using RHF orbitals.

The perpendicular paramagnetic bonding mechanism, which increases the magnitude of the angular momentum of antibonding orbitals, can also be viewed as a mixing of bonding and antibonding orbitals. This is seen in Table V, where, for example, the orbital 1b_u, which corresponds to the antibonding 1s orbital σ_{1s}^* in the parallel orientation, acquires increasingly strong bonding character in stronger fields and at longer bond distances. From the listed mean absolute s values in Table V, we note that the s values decrease with increasing field strength and increasing bond distance. Indeed, strong magnetic fields compress the orbitals and change the relevant length

scale, so that the dissociation limit is reached earlier.

1. Singlet potential-energy curves at $B = 0.2B_0$

Singlet dissociation curves at field strength $B = 0.2B_0$ are shown in Fig. 6 with information given in Table III. In the parallel orientation at $R = 2a_0$, the lowest singlet is dominated by the electron configuration $^1\Sigma_g(\sigma_{1s}^2\sigma_{1s}^{*2})$. The first excited state is $^1\Pi_g(\sigma_{1s}^2\sigma_{1s}^*\pi_{-1})$ with $\Lambda_B = -1$, while second and third states are $^1\Pi_u(\sigma_{1s}^2\sigma_{1s}^*\sigma_{2s})$ and $^1\Sigma_g(\sigma_{1s}^2\sigma_{1s}^*\sigma_{2s}^*)$ with $\Lambda_B = 0$ and the same dissociation limits. All three excited states are covalently bound with approximately the same equilibrium distance of about $2a_0$, whereas the ground state has a shallow minimum at $5.7a_0$.

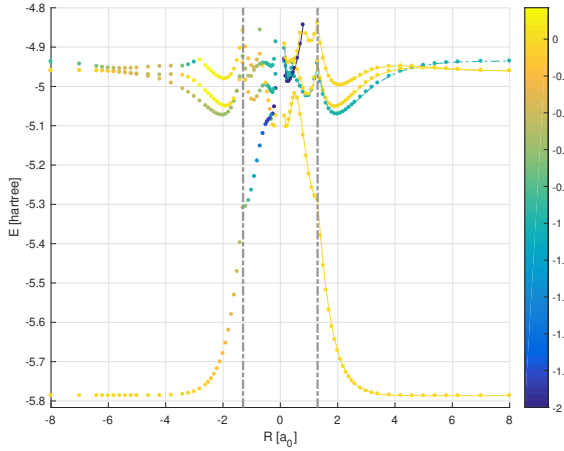


FIG. 6. Dissociation curves for singlet states in perpendicular (negative half) and parallel (positive half) magnetic field $B = 0.2B_0$. In the region between grey dashed lines, the curve is shifted by the nuclear repulsion energy and an additional quadratic fit to align the united atom limit to the same energy scale. Plot markers are coloured based on the AQAM value Λ_B ; scale indicated on the right.

The perpendicular orientation gives rise to dissociation curves that are visually similar. However, the identification of the states requires care since broken symmetries allow mixing of states that are distinct in the parallel case. Moreover, viewed as hypersurfaces that depend on (R, θ, B) , states can be continuously deformed into each other in a way that is sometimes path dependent due to the presence of conical intersections.

At $R = 2a_0$ in the perpendicular orientation, the ground state is $^1A_g(1a_g^21b_u^2)$ and the lowest three singlet excited states are $^1A_g(1a_g^21b_u2b_u)$, $^1B_u(1a_g^21b_u2a_g)$ and $^1B_g(1a_g^21b_u1a_u)$, the latter state being replaced by $^1B_u(1a_g^21b_u3a_g)$ at greater bond distances. The ground state has the same parallel and perpendicular dissociation limits but different parallel and perpendicular united-atom limits, tending to the $1s^22s^2$ beryllium con-

figuration with $\Lambda_B = 0$ in the parallel orientation but to $1s^22p_{-1}^2$ with $\Lambda_B = -2$ in the perpendicular orientation. The first excited state in the perpendicular orientation has $\Lambda_B = -0.6$ arising from the antibonding orbital $1b_u$ and the intermediate orbital $2b_u$, slightly less than the $\Lambda_B = -1.0$ of the first excited state in the parallel orientation (for short bond distances), arising from the singly occupied π_{-1} orbital.

However, as seen in Fig. 7, for a fixed $R = 2$ bohr, the first excited states in the parallel configuration smoothly turn into the corresponding perpendicular states as the angle θ is varied. In particular, the antibonding orbital σ_{2s}^* transforms smoothly into π_{-1} , both being of a_u symmetry in skew orientations. We note that the first excited state has a minimum at $\theta \approx 40^\circ$, which happens since the state a skew angles involves from $^1\Pi_g(\sigma_{1s}^2\sigma_{1s}^*\pi_{-1})$, where σ_{1s}^* and π_{-1} prefer perpendicular and parallel orientations, respectively.

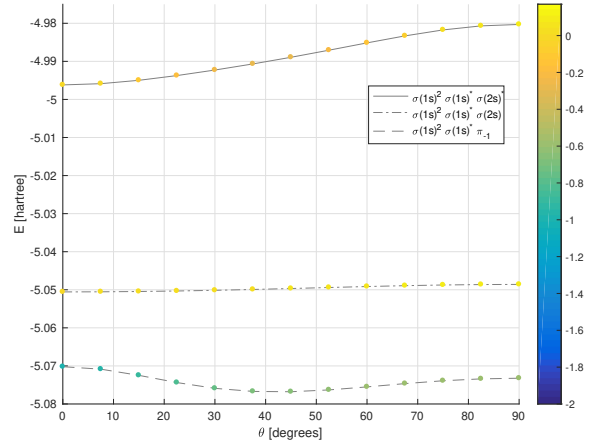


FIG. 7. Energies of singlet excited states as a function of angle θ between the bond axis and magnetic field, with magnitudes fixed at $R = 2a_0$ and $B = 0.2B_0$, respectively.

The second and third excited state have $\Lambda_B \approx 0.1$ in the perpendicular orientation. The second excited state also retains the same radial dissociation limit as the corresponding parallel state, while the third excited state acquires a different dissociation limit due to symmetry breaking and orbital mixing. Globally, this indicates conical intersections on the energy surfaces.

In the given basis set, the ground state is bound by about 50 microhartree in the perpendicular configuration and 30 microhartree in the parallel orientation. Hence, at this field strength, perpendicular paramagnetic bonding is negligible in the ground state. In the first excited state, the energy is lowered by 3 millihartree from parallel to perpendicular orientation. However, the dissociation limit is lowered too, leading to a reduction in radial binding energy from 0.14 hartree to 0.11 hartree. By contrast, the second excited state is essentially unchanged and the third excited state is higher by 16 millihartree in the

perpendicular orientation.

2. Singlet potential-energy curves at $B = B_0$

Potential-energy curves for singlet states at $B = B_0$ are shown in Fig. 8. In the parallel orientation, the weakly bound ground state is dominated by the ${}^1\Sigma_g(\sigma_{1s}^2\sigma_{1s}^{*2})$ configuration at all bond distances, just as for field strength $B = 0.2B_0$. Because of the orbital Zeeman effect, the first and second excited states have substantial π character with $\Lambda_{\mathbf{B}} = -1$, being predominantly ${}^1\Pi_g(\sigma_{1s}^2\sigma_{1s}^*\pi_{-1})$ and ${}^1\Pi_u(\sigma_{1s}^{*2}\sigma_{1s}\pi_{-1})$, respectively. The latter state is obtained from the former by promoting one electron from the σ_{1s} bonding orbital to σ_{1s}^* antibonding orbital. The two states therefore dissociate to the same limit but bind in different ways. The first state is covalently bound with a deep energy minimum at $R = 1.80a_0$, while the second is weakly bound with a shallow minimum at $R = 4.42a_0$. The third excited state has δ character, being predominantly ${}^1\Delta_g(\sigma_{1s}^{*2}\sigma_{1s}\delta_{-2})$ with $\Lambda_{\mathbf{B}} = -2$ and a minimum at $R = 1.89a_0$. We note that the ${}^1\Sigma_u(\sigma_{1s}^2\sigma_{1s}^*\sigma_{2s})$ and ${}^1\Sigma_g(\sigma_{1s}^2\sigma_{1s}^*\sigma_{2s}^*)$ states, which were the second and third excited states at $B = 0.2B_0$, are not stabilized by the orbital Zeeman interaction and have therefore been pushed high up in the spectrum by its diamagnetic interaction with the magnetic field.

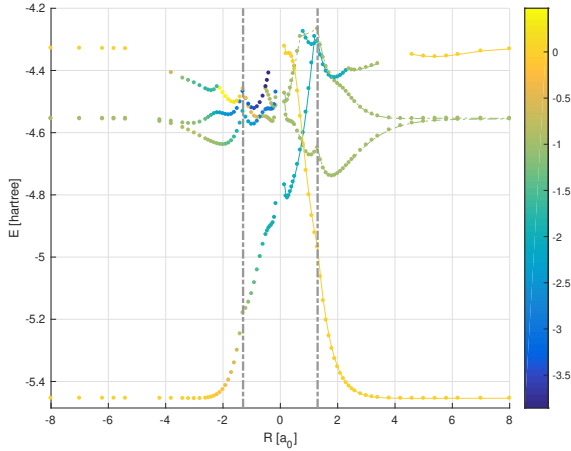


FIG. 8. Dissociation curves for singlet states in perpendicular (negative half) and parallel (positive half) magnetic field $B = B_0$.

The dissociation curves in the perpendicular field orientation are substantially different from those in the parallel orientation. However, since the dissociation limits are identical in the two orientations, the curves become increasingly similar with increasing bond distance. The ground state ${}^1A_g(1a_g^21b_u^2)$, originating from the field-free state ${}^1\Sigma_g^+(\sigma_{1s}^2\sigma_{1s}^{*2})$, is stabilized by perpendicular paramagnetic bonding by about 1 millihartree, with equilibrium bond distance $R = 3.01$ bohr, which is 1.4 bohr

shorter than the bond distance in the parallel field orientation. While the parallel and perpendicular ground states share the same dissociation limit, they tend to different states in the united atom limit—the parallel state becomes ${}^1\Sigma_g(1s^22s^2)$, while the perpendicular state becomes ${}^1\Sigma_g(1s^22p_{-1}^2)$.

In the perpendicular orientation, the lowest three singlet excited states are ${}^1B_u(1a_g^21b_u2a_g)$, ${}^1A_g(1a_g^21b_u2b_u)$, and ${}^1B_g(1a_g^21b_u1a_u)$ at $R = 1.8a_0$; at $R = 3a_0$, the lowest states are ${}^1B_u(1a_g^21b_u2a_g)$, ${}^1A_g(1b_u^21a_g2a_g)$, and ${}^1B_g(1a_g^21b_u2b_u)$. Thus, while the first excited state retains its overall symmetry and orbital occupation at all distances beyond $R = 1.8$ bohr, the second state retains the overall symmetry but changes orbital character and the third state undergoes a level crossing with a state of different symmetry.

It is interesting to compare the first excited states in the two orientations. In the parallel orientation, the first excited state is predominantly ${}^1\Pi_g(\sigma_{1s}^2\sigma_{1s}^*\pi_{-1})$ of bond order one and a half and a deep minimum at $R = 1.80a_0$. In the perpendicular orientation, the ${}^1B_u(1a_g^21b_u2a_g)$ is best described as having orbital configuration $\sigma_{1s}^2\sigma_{1s}^*\pi_{\perp}^*$, with an antibonding HOMO orbital π_{\perp}^* replacing π_{-1} . Whereas the orbital Zeeman interaction favours π_{-1} in the parallel field orientation, it favours π_{\perp}^* in the perpendicular orientation, by the same mechanism that generates paramagnetic bonding. The reduced bond order of one in the perpendicular orientation gives a shallower minimum at a longer bond length $2.01a_0$ compared with the parallel orientation. We note that the first excited state has $\Lambda_{\mathbf{B}} = -1.3$ at the energy minimum, indicating that it has acquired some δ character. In the united-atom limit, the perpendicular state acquires even more δ character, as shown by the colour coding in Fig. 8.

The second excited state has a double minimum in the perpendicular orientation. The global minimum occurs at $R = 3.14a_0$ with $\Lambda_{\mathbf{B}} = -1.1$, indicating some δ character. The orbital occupation in this region of the dissociation curve is $\sigma_{1s}^{*2}\sigma_{1s}\pi_{\perp}^*$, with a negative bond order and a strong paramagnetic bonding (more than an order of magnitude stronger than in the ground state) generated by three electrons occupying antibonding orbitals.

The local minimum in the second excited state occurs at the shorter distance of $R = 1.81a_0$ and has $\Lambda = -2.5$, indicating a substantial increase in δ character. Compared with the second excited state in the parallel orientation, the energy is much lower (by $0.1E_h$ at $R = 2a_0$). Hence, the perpendicular paramagnetic bonding effect is orders of magnitude stronger than in the ground state.

The global picture of the singlet energy surfaces is complicated by level crossings at intermediate bond distances. Rotation of the first and second excited states at a fixed bond distance of $R = 2a_0$ leads to a crossing at roughly 45° , even though the resulting perpendicular states share the same dissociation limit. Hence, at this bond distance, the strongly bound parallel state $\sigma_{1s}^2\sigma_{1s}^*\pi_{-1}$ is rotated into a state near the higher minimum on the second excited perpendicular dissociation

curve. The very weakly bound second excited state, with $\sigma_{1s}^* \sigma_{1s} \pi_{-1}$ character, in the parallel orientation is consequently rotated into the more strongly bound first excited state in the perpendicular orientation.

3. Triplet potential-energy curves at $B = 0.2B_0$

The lowest triplet states at $B = 0.2B_0$ are shown in Fig. 9. As in the field-free case, the triplet He_2 dissociation curves display many features that are analogous to the singlet curves. Equilibrium bond distances are roughly 2 bohr. Moreover, there are again conical intersections connecting low-lying states.

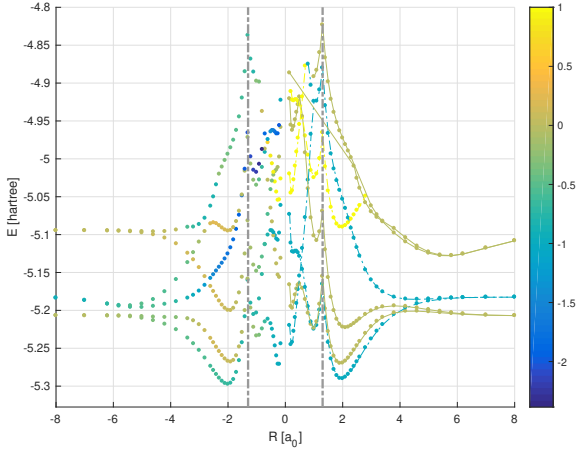


FIG. 9. Dissociation curves for triplet states in perpendicular (negative half) and parallel (positive half) magnetic field $B = 0.2B_0$. In the region between grey dashed lines, the curve is shifted by the nuclear repulsion energy and an additional quadratic fit to align the united atom limit to the same energy scale. Plot markers are coloured based on the AQAM value $\Lambda_{\mathbf{B}}$; scale indicated on the right.

In the parallel orientation at $R = 2a_0$, the lowest triplet is predominantly ${}^3\Pi_g(\sigma_{1s}^2\sigma_{1s}^*\pi_{-1})$ with $\Lambda_{\mathbf{B}} = -1$. The second and third triplet states have $\Lambda_{\mathbf{B}} = 0$ and pure σ character, with configurations predominantly $\sigma_{1s}^2\sigma_{1s}^*\sigma_{2s}$ and $\sigma_{1s}^2\sigma_{1s}^*\sigma_{2s}^*$, respectively. The fourth triplet state at $R = 2a_0$ is related to the first triplet by reversed sign of the angular momentum, having $\Lambda_{\mathbf{B}} = +1$ and an electron configuration dominated by $\sigma_{1s}^2\sigma_{1s}^*\pi_{+1}$. However, at slightly longer bond distances, the fourth triplet state is instead one with $\Lambda_{\mathbf{B}} = -1$ and configuration $\sigma_{1s}^2\sigma_{1s}^*\pi_{-1}^*$, which shares the same dissociation limit as the triplet ground state at $R = 2a_0$.

Fixing the bond distance at $R = 2a_0$ (close to the equilibrium bond distances of the lowest triplet states in all field orientations) and plotting the energies as function of the angle θ between the bond axis and the field vectors, we obtain the curves in Fig. 10. In the perpendicular orientation at this bond distance, the lowest triplet is predominantly ${}^3A_g(1a_g^21b_u2b_u)$, where the σ_{2s}^* HOMO of

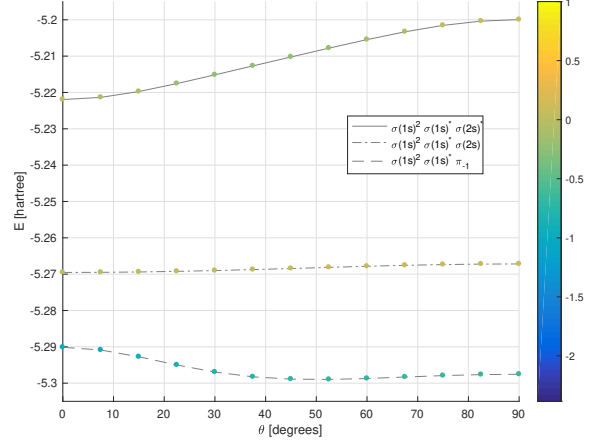


FIG. 10. Energies of the lowest triplet states at $R = 2a_0$ and $B = 0.2B_0$ plotted against the angle θ between the bond axis and magnetic axis

b_u symmetry has evolved smoothly from the π_{-1} HOMO in the parallel orientation, both being of a_u symmetry in skew orientations. In the process, the AQAM projection has decreased from -1 in the parallel orientation to -0.7 in the perpendicular orientation. This lowest triplet state has a preferred field orientation of about 50° , a compromise between the preferred perpendicular orientation of the antibonding σ orbitals and preferred parallel orientation of the π orbital, in the same way as for singlet states in Fig. 7. The energy of the lowest triplet is about 7 millihartree lower in the perpendicular orientation than in the parallel orientation, by paramagnetic stabilization of the antibonding orbitals. However, since the paramagnetic stabilization also lowers the dissociation limit, the bond is actually weaker in the perpendicular orientation.

Even though ${}^3\Pi_g(\sigma_{1s}^2\sigma_{1s}^*\pi_{-1})$ and ${}^3A_g(1a_g^21b_u2b_u)$ are the lowest parallel and perpendicular triplet states at a bond distance of $2a_0$, smoothly connected to each other by field rotation, they have different radial dissociation limits, the latter having the same dissociation limit as the parallel states ${}^3\Sigma_u(\sigma_{1s}^2\sigma_{1s}^*\sigma_{2s})$ and ${}^3\Sigma_g(\sigma_{1s}^2\sigma_{1s}^*\sigma_{2s}^*)$. The ${}^3\Pi_g$ state, on the other hand, crosses the ${}^3\Sigma_u$ and ${}^3\Sigma_g$ states around $R = 4a_0$, dissociating into states of higher energy. and the minimum at $R = 2.1a_0$ is thus a manifestation of the perpendicular paramagnetic bonding mechanism.

The second triplet state in Fig. 10 changes smoothly from ${}^3\Sigma_u(\sigma_{1s}^2\sigma_{1s}^*\sigma_{2s})$ to ${}^3B_u(1a_g^21b_u2a_g)$ from the parallel to the perpendicular orientation, increasing its energy slightly and its AQAM projection from zero to 0.1. The third triplet state changes more dramatically (but smoothly) from ${}^3\Sigma_g(\sigma_{1s}^2\sigma_{1s}^*\sigma_{2s}^*)$ to ${}^3B_g(1a_g^21b_u1a_u)$ as the HOMO changes from σ_{2s}^* to π_u character. Its energy increases by about 20 millihartree, while its AQAM projection first decreases to -0.2 at $\theta \approx 40^\circ$, after which it increases to 0.1 in the perpendicular orientation.

To summarize, the three lowest triplet states at $R = 2a_0$ differ in their HOMOs, which, in order of increasing energy, are $\pi_{-1} < \sigma_{2s} < \sigma_{2s}^*$ in the parallel field orientation (by paramagnetic stabilization of π_{-1}) and $\sigma_{2s}^* < \sigma_{2s} < \pi_{-1}$ in the perpendicular orientation (by paramagnetic stabilization of σ_{2s}^*). We note that, even though the π and σ_{2s}^* orbitals are of different symmetries in the parallel and perpendicular field orientations, they are of the same symmetry in skew orientations and may therefore transform smoothly into each other.

We consider next the electronic states closer to the dissociation limit, at $R = 5a_0$. In Fig. 9, there are three distinct pairs of states both in the parallel field orientation and in the perpendicular orientation—in Fig. 11, we have plotted the energies of the corresponding states against the angle θ at the fixed bond distance $R = 5a_0$. Each pair consists of two close-lying states with the same dissociation limit but of different symmetries (gerade and ungerade) arising from different occupations of bonding and antibonding orbitals. Since we are close to the dissociation limit, the electronic states are typically multiconfigurational, with large contributions from two configurations. We consider the lowest pair of electronic states first.

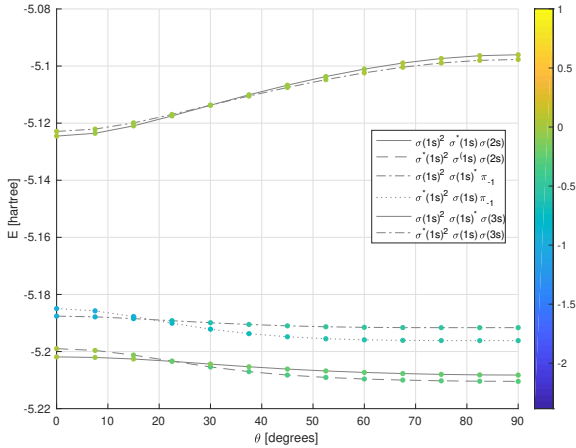


FIG. 11. Triplet states as a function of angle between the bond axis and magnetic field, with magnitudes fixed at $R = 5a_0$ and $B = 0.2B_0$, respectively.

At $R = 5a_0$, the lowest parallel state is predominantly ${}^3\Sigma_u(\sigma_{1s}^2\sigma_{1s}^*\sigma_{2s})$ with one occupied antibonding orbital, while the next state ${}^3\Sigma_g(\sigma_{1s}^2\sigma_{1s}^*\sigma_{2s}^*,\sigma_{1s}^2\sigma_{1s}^*\sigma_{2s})$ has large contributions from two configurations, both with two occupied antibonding orbitals. Although these close-lying states have nearly reached their radial dissociation limits at this bond distance, both are lowered in energy as the angle is increased to 90° , by paramagnetic stabilization of the antibonding orbitals in the nonparallel field. With two occupied antibonding orbitals, the energy lowering is larger for the ${}^3\Sigma_g$ state, which becomes the lowest state at 22° . For this state, the AQAM projection changes

from zero in the parallel field orientation to -0.3 in the perpendicular orientation; for the ${}^3\Sigma_u$ state, the AQAM projection changes less. In the perpendicular field orientation, the symmetries of the states are 3A_g for the lower-energy state and 3B_u for the higher state.

The next pair of states are ${}^3\Pi_g(\sigma_{1s}^2\sigma_{1s}^*\pi_{-1},\sigma_{1s}^2\sigma_{1s}^*\pi_{-1}^*)$ and ${}^3\Pi_u(\sigma_{1s}^2\sigma_{1s}^*\pi_{-1},\sigma_{1s}^2\sigma_{1s}^*\pi_{-1}^*)$ in the parallel orientation, both with more weight on the configuration containing the bonding orbital π_{-1} . The ${}^3\Pi_u$ state is slightly higher in energy, have a doubly occupied σ_{1s}^* orbital in the dominant configuration. As a result of paramagnetic stabilization, the gerade and ungerade states cross at about $\theta = 30^\circ$. Furthermore, with increasing θ , the configurations containing the antibonding orbital π_{-1}^* (originating from π_{-1}^*) become more important than the configurations containing π_{-1} . In the perpendicular orientation, the dominant configurations are ${}^3B_u(1a_g^21b_u3a_g)$ and ${}^3A_g(1b_u^21a_g3a_g)$ where $3a_g$ is the π_{-1}^* orbital. Both states have minima at roughly $R = 5a_0$, which are manifestations of perpendicular paramagnetic bonding.

Notably, there are indications of perpendicular paramagnetic bonding also in states of higher angular momentum. Tracing the third triplet state at $R = 5a_0$ in the perpendicular orientation to shorter bond distances, we find that it develops an AQAM value of -1.5 at $R \approx 2a_0$, implying that it has acquired some δ -orbital character, although the orbital Zeeman effect due to the larger magnitude of the angular momentum is not enough to offset other effects, in particular the electrostatic repulsion, at these bond lengths.

4. Triplet potential-energy curves at $B = B_0$

At $B = B_0$, the two lowest parallel electronic states, both with $\Lambda_B = -1$, have the same dissociation limit and are energetically well separated from the other states. The lower state is dominated by a single electron configuration ${}^3\Pi_g(\sigma_{1s}^2\sigma_{1s}^*\pi_{-1})$, while the higher ${}^3\Pi_u$ state is more mixed, with weights 66% on $\sigma_{1s}^2\sigma_{1s}^*\pi_{-1}^*$ and 29% on $\sigma_{1s}^2\sigma_{1s}^*\pi_{-1}$ at $R = 2a_0$.

The spectrum above these states is more complicated, with states closer together and crossings in the interval $2a_0 \leq R \leq 4a_0$. At $R = 2a_0$, the third electronic state is ${}^3\Delta_u(\sigma_{1s}^2\sigma_{1s}^*\delta_{-2})$ with $\Lambda_B = -2$, while the fourth state is ${}^3\Sigma_u(\sigma_{1s}^2\sigma_{1s}^*\sigma_{2s})$ with $\Lambda_B = 0$. The fifth state is again a mixed ${}^3\Pi_u$ state with $\Lambda_B = -1$; it has the same dominant configurations as the second state but with weights 65% on $\sigma_{1s}^2\sigma_{1s}^*\pi_{-1}$ and 29% on $\sigma_{1s}^2\sigma_{1s}^*\pi_{-1}^*$. The sixth state is ${}^3\Sigma_g(\sigma_{1s}^2\sigma_{1s}^*\sigma_{2s}^*)$ with $\Lambda_B = 0$.

Tracking the lowest two states from the parallel orientation through a 90° rotation is straightforward. As seen in Fig. 13, at a fixed bond distance of $R = 2a_0$, the states cross at about 40° . The bound parallel state ${}^3\Pi_g(\sigma_{1s}^2\sigma_{1s}^*\pi_{-1})$ is deformed into a nearly unbound, dissociative state ${}^3A_g(1a_g^21b_u2b_u)$ on the perpendicular side as the bonding π_{-1} orbital transforms into the antibonding σ_{2s}^* orbital. There is, however, a minimum at the

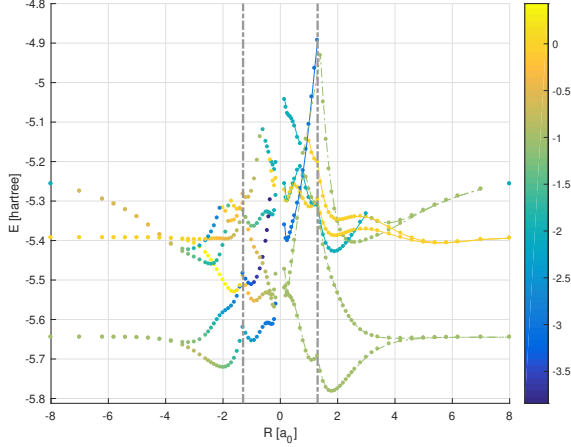


FIG. 12. Dissociation curves for triplet states in perpendicular (negative half) and parallel (positive half) magnetic field $B = B_0$.

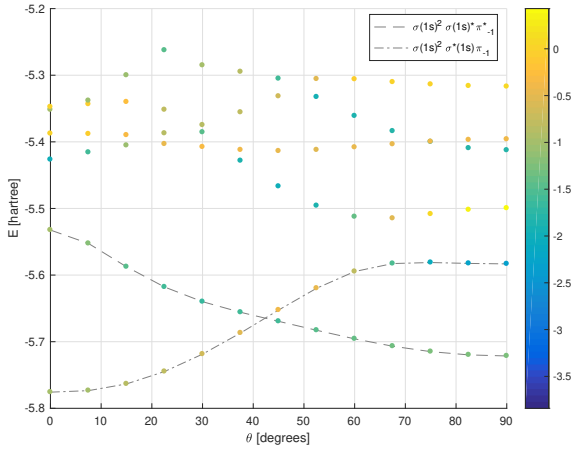


FIG. 13. Triplet states as a function of angle between the bond axis and magnetic field, with magnitudes fixed at $R = 2a_0$ and $B = B_0$, respectively.

larger bond distance of $R = 3.2a_0$, with $\Lambda_{\mathbf{B}} = -1.1$ and a depth of 14 millihartree, for this state, in part generated by paramagnetic bonding. At the same time, the unbound parallel state dominated by ${}^3\Pi_u(\sigma_{1s}^2\sigma_{1s}^*\pi_{-1}^*)$ transforms into the ${}^3B_u(1a_g^21b_u2a_g)$ with $\Lambda_{\mathbf{B}} = -1.25$, which is bound by perpendicular paramagnetic bonding. Compared with the parallel orientation, the energy difference is almost 0.2 hartree—a manifestation of very strong perpendicular paramagnetic bonding. However, this state is not the global minimum over all triplet states and geometries, which instead occurs in the parallel orientation.

5. Quintet potential-energy curves at $B = 0.2B_0$

Dissociation curves for quintet states subject to a field $B = 0.2B_0$ are shown in Fig. 14. In the parallel orientation, the lowest-lying parallel states at $R = 4.2a_0$ alternate between $\Lambda_{\mathbf{B}} = -1$ and $\Lambda_{\mathbf{B}} = 0$. The lowest quintet state is predominantly ${}^5\Pi_g(\sigma_{1s}\sigma_{1s}^*\sigma_{2s}\pi_{-1})$ and covalently bound, while the second quintet is multiconfigurational ${}^5\Sigma_g(0.53\sigma_{1s}\sigma_{1s}^*\sigma_{2s}\sigma_{2s}^*, 0.21\sigma_{1s}\sigma_{1s}^*\sigma_{2s}^*\sigma_{2p})$ and non-covalently bound. The third and fourth parallel quintets at $R = 4.2a_0$ are predominantly ${}^5\Pi_u(\sigma_{1s}\sigma_{1s}^*\sigma_{2s}^*\pi_{-1})$ and ${}^5\Sigma_u(\sigma_{1s}\sigma_{1s}^*\sigma_{2s}\sigma_{2p})$, respectively.

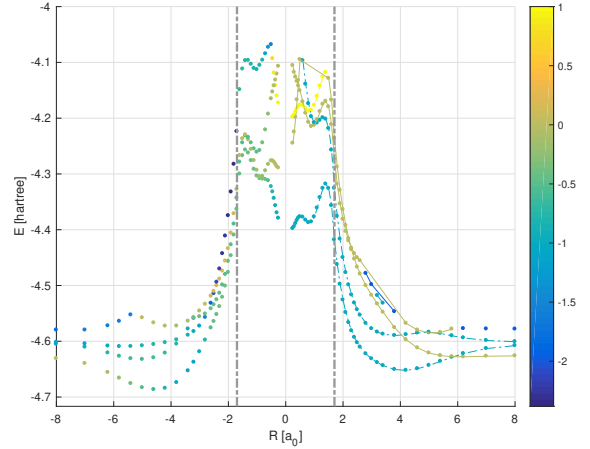


FIG. 14. Dissociation curves for quintet states in perpendicular (negative half) and parallel (positive half) magnetic field $B = 0.2B_0$.

When rotated from parallel ($\theta = 0^\circ$) to perpendicular ($\theta = 90^\circ$) orientation at the slightly shorter bond length of $R = 3.8a_0$, the lowest quintet state does not undergo any level crossing; see Fig. 15. From the parallel to the perpendicular orientation, the binding HOMO π_{-1} transforms into the antibonding σ_{2s}^* orbital of symmetry b_u , while the antibonding π_{-1}^* of a_g symmetry is stabilized paramagnetically. The resulting lowest perpendicular state becomes ${}^5A_g(0.441a_g1b_u2b_u3a_g, 0.271a_g1b_u2b_u2a_g)$ where the dominant configuration has more occupied antibonding than bonding orbitals. Nevertheless, because of paramagnetic stabilization of antibonding orbitals, the total energy decreases by more than 20 millihartree, while the dissociation energy increases from 48 to 59 millihartree as the covalent bond in the parallel orientation is replaced by a paramagnetic bond in the perpendicular orientation. Considering the relatively small magnitude of the magnetic field in this case, this provides an example of paramagnetic bonding that is orders of magnitude stronger than the initially reported bonding in the lowest H_2 triplet and He_2 singlet states [28].

As we go from the parallel to perpendicular field orientation, the AQAM projection of the lowest state de-

creases in magnitude, from -1 to -0.8 , providing another example where this quantity does not directly capture the energy stabilization by the orbital Zeeman interaction. However, the radial dissociation limits are different in the parallel and perpendicular orientations, with the latter corresponding to two helium atoms in the $1s2s$ triplet state. Hence, from this perspective, the AQAM value changes from zero in the perpendicular radial dissociation limit to about -0.7 at the minimum, correctly indicating a stabilizing orbital Zeeman effect compared to the dissociation limit.

At $R = 3.8a_0$, the second and third quintet states in the parallel orientation are ${}^5\Pi_u$ and ${}^5\Sigma_g^+$, respectively. As seen from Fig. 15, these states undergo two level crossings from the parallel to perpendicular orientation, at about 20 and 70 degrees. The double crossing arises since ${}^5\Sigma_g^+$ has an energy minimum at about 45 degrees, while ${}^5\Pi_u$ has a maximum at about 35 degrees. We note that ${}^5\Sigma_g^+$ develops a substantial AQAM projection of -0.8 at 90 degrees and is even close to -1.1 at intermediate angles of 30–40 degrees (i.e., near the energy minimum). Both states have a lower energy at 90 degrees than at 0 degrees, with configurations ${}^5B_u(1a_g1b_u2a_g3a_g)$ and ${}^5A_g(0.391a_g1b_u2b_u2a_g, 0.321a_g1b_u2b_u3a_g)$, respectively.

The fourth perpendicular quintet state at $R = 3.8a_0$ is ${}^5B_g(0.491a_g1b_u2a_g1a_u, 0.331a_g1b_u3a_g1a_u)$. However, after a level crossing at $R = 5.8a_0$, the fourth state is ${}^5A_g(0.551a_g1b_u3a_g3b_u, 0.301a_g1b_u2a_g3b_u)$.

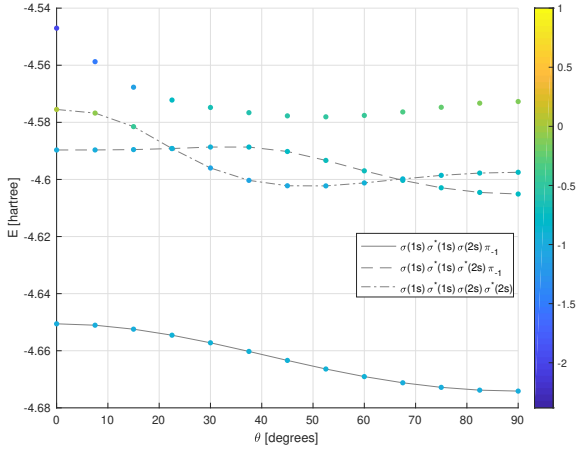


FIG. 15. Energies of the lowest quintet states as a function of angle between the bond axis and magnetic field, with magnitudes fixed at $R = 3.8a_0$ and $B = 0.2B_0$, respectively.

6. Quintet potential-energy curves at $B = B_0$

At a field strength of $B = B_0$, the orbital Zeeman interaction has rearranged the states so that all the states containing only σ orbitals are well above those that con-

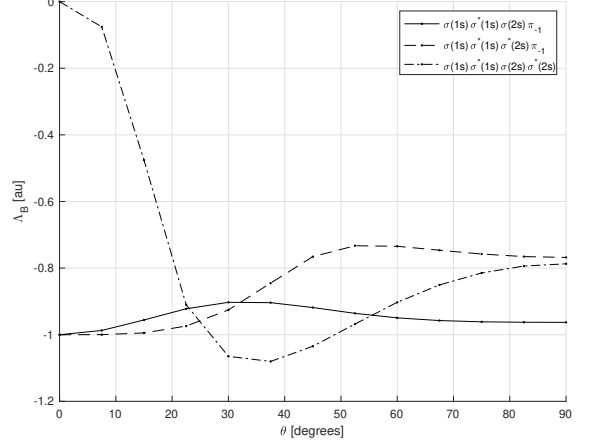


FIG. 16. AQAM value for the lowest quintet states as a function of angle between the bond axis and magnetic field, with magnitudes fixed at $R = 3.8a_0$ and $B = 0.2B_0$, respectively.

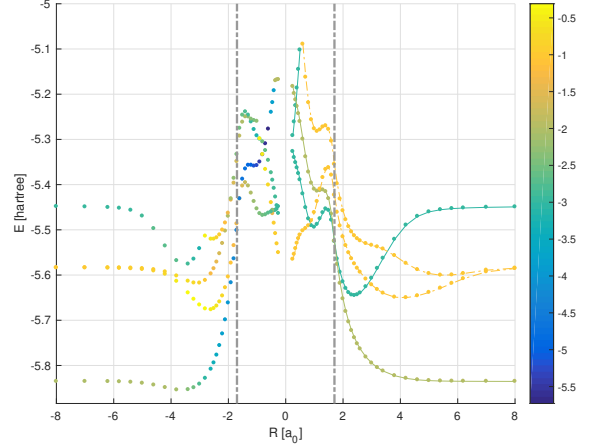


FIG. 17. Dissociation curves for quintet states in perpendicular (negative half) and parallel (positive half) magnetic field $B = B_0$.

tain π orbitals. The lowest parallel state is dominated by the ${}^5\Delta_g(\sigma_{1s}\sigma_{1s}^*\pi_{-1}\pi_{-1}^*)$ configuration, which is well below all other states for all bond lengths greater than $2a_0$. At a bond distance of $R = 4.2a_0$, the second quintet state is dominated by the ${}^5\Pi_g(\sigma_{1s}\sigma_{1s}^*\pi_{-1}\sigma_{2s})$ configuration, while the third quintet state is multiconfigurational ${}^5\Pi_u(0.69\sigma_{1s}\sigma_{1s}^*\pi_{-1}^*\sigma_{2s}, 0.22\sigma_{1s}\sigma_{1s}^*\pi_{-1}\sigma_{2s}^*)$. The fourth quintet state is largely ${}^5\Phi_g(\sigma_{1s}\sigma_{1s}^*\pi_{-1}\delta_{-2})$.

In the perpendicular field orientation at field strength $B = B_0$, the lowest quintet states at bond distance $R = 3.8a_0$ are ${}^5A_g(1a_g1b_u2a_g2b_u)$, ${}^5B_g(1a_g1b_u2a_g1a_u)$, and ${}^5A_u(0.711a_g1b_u2a_g1b_g, 0.211a_g1b_u2b_u1a_u)$. The fourth quintet state is ${}^5B_u(1a_g1b_u2a_g3a_g)$; however, at a shorter bond distance of $R = 2.5a_0$, the fourth state has undergone a level crossing and is of the symmetry

${}^5A_g(1a_g1b_u2a_g3b_u)$.

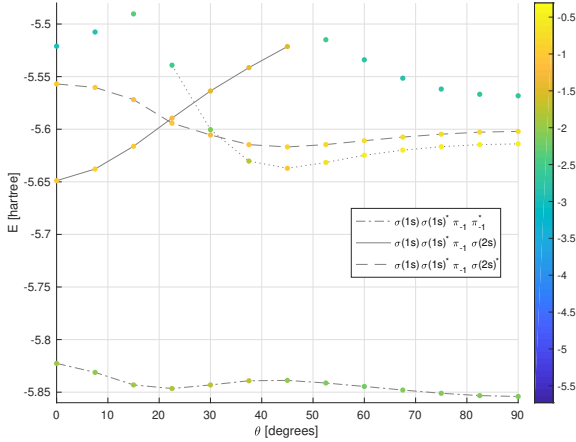


FIG. 18. Quintet states as a function of angle between the bond axis and magnetic field, with magnitudes fixed at $R = 3.8a_0$ and $B = B_0$, respectively.

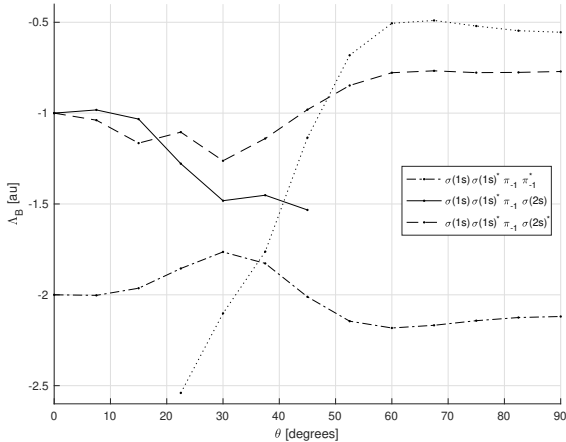


FIG. 19. AQAM value for the lowest quintet states as a function of angle between the bond axis and magnetic field, with magnitudes fixed at $R = 3.8a_0$ and $B = B_0$, respectively.

Rotation of the parallel states into perpendicular states is comparatively straightforward due to the energy separations between the dissociation curves—see Fig. 18 for rotation at the bond distance $R = 3.8a_0$. The lowest state ${}^5\Delta_g(\sigma_{1s}\sigma_{1s}^*\pi_{-1}\pi_{-1}^*)$ is further lowered by about 30 millihartree from 0 to 90 degrees. It is paramagnetically bound, with a dissociation energy of 20 millihartree and a global minimum located at $\theta = 90^\circ$ and a slightly shorter bond distance $R = 3.62a_0$.

Intriguingly, the rotation curve in Fig. 18 has a second local minimum with respect to θ at about 25° . The corresponding AQAM values in Fig. 19 show that this local minimum is not associated with any increase in the mag-

nitude $|\Lambda_B|$. The stabilization at $\theta \approx 25^\circ$ is therefore of a different origin than the stabilization at $\theta = 90^\circ$.

IV. ENERGY SURFACES

Complete energy surfaces for the lowest singlet, triplet, and quintet states at $B = B_0$ are shown in Fig. 20, 21, and 23, respectively. These surfaces have been computed at the FCI/Lu-aug-cc-pVTZ level with a correction for basis-set superposition error (BSSE). The correction is an adapted counterpoise correction, taking into account the loss of symmetry in a magnetic field and, in particular, the inequivalence of the parallel and perpendicular orientations.

The most dramatic feature is seen in the triplet surface in Fig. 21, which is actually at each (R, θ) the minimum of two surfaces. One of these crossing states has a minimum in the perpendicular orientation and the other has a deeper minimum in the parallel orientation. The level crossing is clearly seen as a discontinuous “rift” that occurs for the shorter bond distances and angles roughly between 20° and 50° .

On the singlet surface in Fig. 20 the minimum is located at $R = 3.01a_0$ and $\theta = 90^\circ$ and the BSSE corrected dissociation energy is 1.264 millihartree, which differs only negligibly different from the uncorrected value in Table IV. On the triplet surface in Fig. 21, the deepest minimum occurs at $R = 1.80a_0$ and $\theta = 0^\circ$, with a BSSE corrected dissociation energy of 0.1376 hartree. The shallower minimum occurs at $R = 1.99a_0$ and has a BSSE corrected dissociation energy of 0.07676 hartree, again negligibly different from the uncorrected value. Finally, the quintet surface in Fig. 23 has two minima. The deeper minimum occurs at $R = 3.61a_0$, $\theta = 90^\circ$, and has a BSSE corrected dissociation energy of 19.56 millihartree. The shallower minimum is located at $3.5a_0$ and $\theta = 24^\circ$, with a dissociation energy of 11.7 millihartree.

V. CONCLUSIONS

We have studied the low-lying states of the helium dimer for different spins and magnetic-field strengths. As expected, the singlet, triplet, and quintet spectra resemble each other to a great degree, since many states have analogues with other total spin. For example, open-shell singlets have direct analogues among triplets. In general, all states are subject to a diamagnetic destabilization. However, the spin and orbital Zeeman interactions affect states differently and dramatically reorder the spectra, bringing down states of higher angular momentum. Hence, states with π and δ bonding orbitals become increasingly important in strong fields. Moreover, at large field strengths, the spin Zeeman interaction lowers the $m_s = -1$ triplets below the singlets. For a field strength of $B = B_0$, the globally lowest state is even a paramagnetically bonded quintet state with $D_e = 52$ kJ/mol, ori-

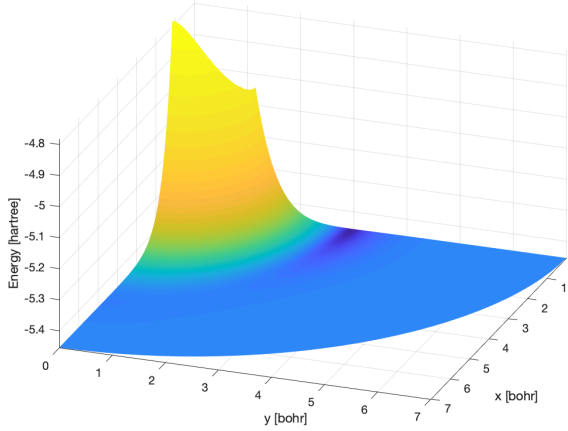


FIG. 20. The lowest singlet energy surface in a field of $B = B_0$. The axis labels are $x = R \cos(\theta)$ and $y = R \sin(\theta)$, so that the left side where $y = 0$ (and $\theta = 0^\circ$) corresponds to the parallel orientation. The colour scale is $\ln(\eta + E(R, \theta) - E_{\min})$, with $\eta = 10^{-4}$ hartree.

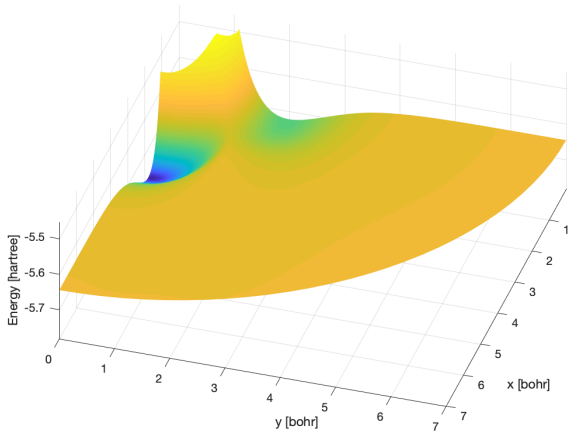


FIG. 21. The lowest triplet energy surface in a field of $B = B_0$. The axis labels are $x = R \cos(\theta)$ and $y = R \sin(\theta)$. The colour scale is $\ln(\eta + E(R, \theta) - E_{\min})$, with $\eta = 5 \times 10^{-3}$ hartree.

ented perpendicular to the magnetic field. Hence, these field strengths induce an entirely new chemistry of helium atoms.

In general, in addition to the effects of increasing field strength, the orientation with respect to the magnetic field modulates the proportion of σ , π and δ bonding, which affects the total angular momentum and the orbital Zeeman interaction. For nontrivial orientations of the bond axis with respect to the magnetic field, all spatial symmetries except inversion are lost and the canonical angular momentum ceases to be a good quantum number. To partially address this complication, we have introduced the almost quantized angular momen-

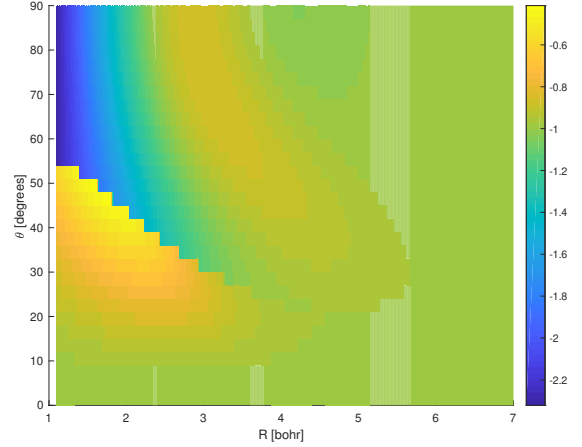


FIG. 22. The AQAM projection onto the magnetic field direction for the lowest triplet at each value of (R, θ) . The level crossing between the two low-lying triplets is clearly manifested in the discontinuous “rift” that begins at $R \approx 1$ bohr and $\theta \approx 50^\circ$.

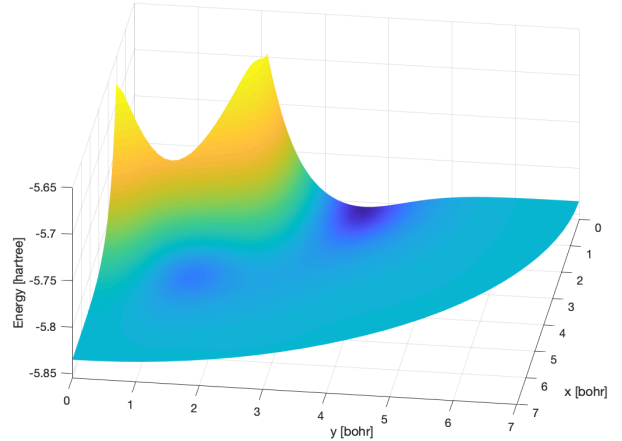


FIG. 23. The lowest quintet energy surface in a field of $B = B_0$. The axis labels are $x = R \cos(\theta)$ and $y = R \sin(\theta)$. The colour scale is $\ln(\eta + E(R, \theta) - E_{\min})$, with $\eta = 5 \times 10^{-3}$ hartree.

tum (AQAM) and demonstrated that it is a very useful tool to characterize states in arbitrary orientations. Conical intersections make detailed state classification beyond the characterization provided by AQAM challenging and poorly defined. In general, energy hypersurfaces become multivalued as functions of the parameters (R, θ, B) . This occurs as an effect of the symmetry breaking, which turns true crossings in the parallel orientation into avoided crossings at nontrivial angles. Two states may be continuously deformed into each other along some paths in parameter space, but not others. In the radial dissociation limit, for instance, the parallel and perpendicular orientations become physically equivalent.

Nonetheless, at a fixed bond distance, continuously deforming between the parallel and perpendicular orientations can result in a state with a different radial dissociation limit.

Our results show that perpendicular paramagnetic bonding is common in excited electronic states, although the presence of conical intersections makes the identification somewhat poorly defined and dependent on the which path in parameter space is emphasized. Moreover, the effect is larger for the more diffuse σ_{2s}^* compared to the compact σ_{1s}^* orbital. As a result, the bonding mechanism is also stronger, sometimes by orders of magnitudes, in excited states than the originally described cases (lowest triplet of H_2 and lowest singlet of He_2). There are some indications of the perpendicular paramagnetic bonding mechanism involving higher angular momentum

states (e.g., modulation of π into δ orbitals or δ into ϕ orbitals), although it is difficult to determine the relative contributions from σ^* and higher angular momentum orbitals.

ACKNOWLEDGMENTS

This work was supported by the Research Council of Norway through Grant No. 240674 and CoE Hylleraas Centre for Molecular Sciences Grant No. 262695. This work has also received support from the Norwegian Supercomputing Program (NOTUR) through a grant of computer time (Grant No. NN4654K).

-
- [1] R. H. Garstang, Rep. Prog. Phys. **40**, 105 (1977).
 [2] D. Lai, Rev. Mod. Phys. **73**, 629 (2001).
 [3] S. Jordan, P. Schmelcher, and W. Becken, Astron. Astrophys. **376**, 614 (2001).
 [4] S. Jordan, P. Schmelcher, W. Becken, and W. Schweizer, Astron. Astrophys. **336**, L33 (1998).
 [5] Y. P. Kravchenko, M. A. Lieberman, and B. Johansson, Phys. Rev. A **54**, 287 (1996).
 [6] O.-A. Al-Hujaj and P. Schmelcher, Phys. Rev. A **61**, 063413 (2000).
 [7] M. D. Jones, G. Ortiz, and D. M. Ceperley, Phys. Rev. A **59**, 2875 (1999).
 [8] W. Becken and P. Schmelcher, Phys. Rev. A **65**, 033416 (2002).
 [9] A. Thirumalai and J. S. Heyl, Phys. Rev. A **79**, 012514 (2009).
 [10] O.-A. Al-Hujaj and P. Schmelcher, Phys. Rev. A **70**, 023411 (2004).
 [11] M. V. Ivanov and P. Schmelcher, Phys. Rev. A **61**, 022505 (2000).
 [12] M. V. Ivanov and P. Schmelcher, Phys. Rev. A **60**, 3558 (1999).
 [13] A. Thirumalai, S. J. Desch, and P. Young, Phys. Rev. A **90**, 052501 (2014).
 [14] A. V. Turbiner and J. C. L. Vieyra, Phys. Rep. **424**, 309 (2006).
 [15] J. Avron, I. Herbst, and B. Simon, Phys. Rev. Lett. **39**, 1068 (1977).
 [16] A. V. Turbiner and N. L. Guevara, J. Phys. B **40**, 3249 (2007).
 [17] A. V. Turbiner and N. L. Guevara, Phys. Rev. A **74**, 063419 (2006).
 [18] J. Ozaki, Chem. Phys. Lett. **203**, 184 (1993).
 [19] P. Schmelcher and L. S. Cederbaum, Phys. Rev. A **41**, 4936 (1990).
 [20] U. Kappes, P. Schmelcher, and T. Pacher, Phys. Rev. A **50**, 3775 (1994).
 [21] T. Detmer, P. Schmelcher, and L. S. Cederbaum, Phys. Rev. A **57**, 1767 (1998).
 [22] T. Detmer, P. Schmelcher, and L. S. Cederbaum, J. Chem. Phys. **109**, 9694 (1998).
 [23] M. Žaucer and A. Ažman, Phys. Rev. A **18**, 1320 (1978).
 [24] Y. E. Lozovik and A. V. Klyuchnik, Phys. Lett. A **66**, 282 (1978).
 [25] S. Basile, F. Trombetta, and G. Ferrante, Il Nuovo Cimento **9**, 457 (1987).
 [26] A. V. Korolev and M. A. Lieberman, Phys. Rev. A **45**, 1762 (1992).
 [27] A. Kubo, J. Phys. Chem. A **111**, 5572 (2007).
 [28] K. K. Lange, E. I. Tellgren, M. R. Hoffmann, and T. Helgaker, Science **337**, 327 (2012).
 [29] E. I. Tellgren, S. S. Reine, and T. Helgaker, Phys. Chem. Chem. Phys. **14**, 9492 (2012).
 [30] S. Stopkowicz, J. Gauss, K. K. Lange, E. I. Tellgren, and T. Helgaker, J. Chem. Phys. **143**, 074110 (2015), <https://doi.org/10.1063/1.4928056>.
 [31] M. Motokawa, Rep. Prog. Phys. **67**, 1995 (2004).
 [32] D. Nakamura, H. Sawabe, Y. H. Matsuda, and S. Takeyama, Rev. Sci. Instrum. **84**, 044702 (2013).
 [33] D. Nakamura, A. Ikeda, H. Sawabe, Y. H. Matsuda, and S. Takeyama, Rev. Sci. Instrum. **89**, 095106 (2018).
 [34] A. Bykov, M. Dolotenko, N. Kolokolchikov, S. V.D., and O. Tatsenko, Physica B **274-275**, 574 (2001).
 [35] B. Murdin, J. Li, M. Pang, E. Bowyer, K. Litvinenko, S. Clowes, H. Engelkamp, C. Pidgeon, I. Galbraith, N. Abrosimov, H. Riemann, S. Pavlov, H.-W. Hübers, and P. Murdin, Nature Comm. **4**, 1469 (2013).
 [36] K. L. Litvinenko, M. Pang, J. Li, E. Bowyer, H. Engelkamp, V. B. Shuman, L. M. Portsel, A. N. Lodygin, Y. A. Astrov, S. G. Pavlov, H.-W. Hübers, C. R. Pidgeon, and B. N. Murdin, Phys. Rev. B **90**, 115204 (2014).
 [37] Y. Kimura and K. Takazawa, Rev. Sci. Instrum. **82**, 013108 (2011).
 [38] T. S. Monteneiro and K. T. Taylor, J. Phys. B **23**, 427 (1990).
 [39] G. I. Pagola, M. C. Caputo, M. B. Ferraro, and P. Lazzeretti, Chem. Phys. Lett. **400**, 133 (2004).
 [40] G. I. Pagola, M. C. Caputo, M. B. Ferraro, and P. Lazzeretti, J. Chem. Phys. **120**, 9556 (2004).
 [41] G. I. Pagola, S. Pelloni, M. C. Caputo, M. B. Ferraro, and P. Lazzeretti, Phys. Rev. A **72**, 033401 (2005).
 [42] G. I. Pagola, M. B. Ferraro, and P. Lazzeretti, J. Chem. Theor. Comp. **5**, 3049 (2009).

- [43] J. Vaara, P. Manninen, and J. Lounila, *Chem. Phys. Lett.* **372**, 750 (2003).
- [44] P. Manninen and J. Vaara, *Phys. Rev. A* **69**, 022503 (2004).
- [45] F. London, *J. Phys. Radium* **8**, 397 (1937).
- [46] H. F. Hamerka, *Mol. Phys.* **1**, 203 (1958).
- [47] R. Ditchfield, *J. Chem. Phys.* **65**, 3123 (1976).
- [48] T. Helgaker and P. Jørgensen, *J. Chem. Phys.* **95**, 2595 (1991).
- [49] E. I. Tellgren, A. Soncini, and T. Helgaker, *J. Chem. Phys.* **129**, 154114 (2008).
- [50] "LONDON, a quantum-chemistry program for plane-wave/GTO hybrid basis sets and finite magnetic field calculations. By E. Tellgren (primary author), T. Helgaker, A. Soncini, K. K. Lange, A. M. Teale, U. Ekström, S. Stopkowicz, J. H. Austad, and S. Sen. See londonprogram.org for more information."
- [51] R. D. Reynolds and T. Shiozaki, *Phys. Chem. Chem. Phys.* **17**, 14280 (2015).
- [52] T. J. P. Irons, J. Zemen, and A. M. Teale, *J. Chem. Theory Comput.* **13**, 3636 (2017), pMID: 28692291, <https://doi.org/10.1021/acs.jctc.7b00540>.
- [53] D. B. Williams-Young, A. Petrone, S. Sun, T. F. Stetina, P. Lestrage, C. E. Hoyer, D. R. Nascimento, L. Koulias, A. Wildman, J. Kasper, J. J. Goings, F. Ding, A. E. DePrince III, E. F. Valeev, and X. Li, *WIREs Computational Molecular Science*, e1436 <https://onlinelibrary.wiley.com/doi/pdf/10.1002/wcms.1436>.
- [54] S. Sun, D. B. Williams-Young, T. F. Stetina, , and X. Li, *J. Chem. Theor. Comp.* **15**, 348 (2019).
- [55] A. Ishikawa, H. Nakashima, and H. Nakatsuji, *Chem. Phys.* **401**, 62 (2012).
- [56] H. Nakashima and H. Nakatsuji, *Astrophys. J.* **725**, 528 (2010).
- [57] E. I. Tellgren and H. Fliegl, *J. Chem. Phys.* **139**, 164118 (2013).
- [58] E. I. Tellgren, A. M. Teale, J. W. Furness, K. K. Lange, U. Ekström, and T. Helgaker, *J. Chem. Phys.* **140**, 034101 (2014).
- [59] J. W. Furness, J. Verbeke, E. I. Tellgren, S. Stopkowicz, U. Ekström, T. Helgaker, and A. M. Teale, *J. Chem. Theory Comput.* **11**, 4169 (2015).
- [60] S. Sen, K. K. Lange, and E. I. Tellgren, *J. Chem. Theor. Comp.* **15**, 3974 (2019).
- [61] E. I. Tellgren, A. Laestadius, T. Helgaker, S. Kvaal, and A. M. Teale, *J. Chem. Phys.* **148**, 024101 (2018).